Mon. Not. R. Astron. Soc. **360,** 253–271 (2005) doi:10.1111/j.1365-2966.2005.09031.x

New photometric and spectroscopic observations of the Seyfert galaxy Mrk 315

S. Ciroi,[1]★† V. L. Afanasiev,[2] A. V. Moiseev,[2] V. Botte,[1]† F. Di Mille,[1] S. N. Dodonov,[2] P. Rafanelli[1] and A. A. Smirnova[2]

[1]*Department of Astronomy, Padova University, Vicolo dell'Osservatorio 2, Padova 35122, Italy*
[2]*Special Astrophysical Observatory, Nizhnij Arkhyz 369167, Russia*

Accepted 2005 March 18. Received 2005 March 7; in original form 2005 January 20

ABSTRACT

We present new important results about the intermediate-type Seyfert galaxy Mrk 315, recently observed through optical imaging and integral-field spectroscopy. Broad-band images were used to study the morphology of the host galaxy, narrow-band Hα images to trace the star-forming regions, and middle-band [O III] images to evidence the distribution of the highly ionized gas. Some extended emission regions were isolated and their physical properties studied by means of flux-calibrated spectra. High-resolution spectroscopy was used to separate different kinematic components in the velocity fields of gas and stars. Some peculiar features characterize this apparently undisturbed and moderately isolated active galaxy. Such features, already investigated by other authors, are re-analysed and discussed in the light of these new observations. The most relevant results we obtained are: the multitiers structure of the disc; the presence of a quasi-ring of regions with star formation much higher than previous claims; a secondary nucleus confirmed by a stellar component kinematically decoupled by the main galaxy; a new hypothesis about the controversial nature of the long filament, initially described as hook shaped, and more likely made of two independent filaments caused by interaction events between the main galaxy and two dwarf companions.

Key words: galaxies: individual: Mrk 315 – galaxies: interactions – galaxies: Seyfert.

1 INTRODUCTION

Understanding the processes responsible for triggering the activity in galactic nuclei is one of the fundamental outstanding questions regarding active galactic nuclei (AGNs). Several mechanisms have been invoked during the last decades, as the presence of circumnuclear star clusters, nuclear bars, discs or spirals, and the interaction between galaxies, in form of close encounters and mergers. Unfortunately, none of them produced conclusive results. For example, nuclear bars and spirals seem not to be more common among AGNs than among non-active galaxies (Carollo, Stiavelli & Mack 1998; Pogge & Martini 2002; Martini et al. 2003). Numerical simulations showed that the gravitational interaction between galaxies can bring gas from the disc toward the nuclear regions (Mihos & Hernquist 1994; Hernquist & Mihos 1995; Mihos & Hernquist 1996). Nevertheless, statistical studies of the large-scale environments of nearby AGNs produced until now controversial results (see e.g. Dahari 1984; Bushouse 1986; Fuentes-Williams & Stocke 1988; MacKenty 1989; Laurikainen et al. 1994; Rafanelli, Violato & Baruffolo 1995; De Robertis, Yee & Hayhoe 1998; Schmitt 2001), and failed to demonstrate that a one-to-one relationship between activity and interaction does really exist. In contrast, deep high-resolution imaging and follow-up spectroscopy of these galaxies allowed to identify merging systems or the presence of close faint companions, suggesting that the investigation of the interaction–activity relation should be addressed to AGN hosts and their immediate surroundings. Therefore, one of the most natural approaches to this topic is looking for effects of interaction in apparently isolated and morphologically undisturbed nearby Seyfert galaxies. In this paper we present new results about the intermediate-type Seyfert galaxy, Mrk 315.

Mrk 315 (II Zw 187) is a well-known active galaxy. Spectroscopically classified as Seyfert 1.5 by Koski (1978), it was studied by Wilson (1988) with high-resolution long-slit scanning of the nuclear and extranuclear regions of the galaxy (within a radius of 5 arcsec). His spectra, obtained around Hβ and [O III] emission lines, revealed the presence of a two distinct kinematic components associated to gas showing different ionization degrees. Mrk 315 was also extensively investigated by MacKenty (1986), MacKenty et al. (1994) and Simkin & MacKenty (2001). These authors found an unusual jet-like ionized gas feature, emitting in the [O III] narrow-band filter

★E-mail: ciroi@pd.astro.it
†Guest Investigator of the UK Astronomy Data Centre.

but not visible in Very Large Array radio maps, and suggested that it was gas drawn out from Mrk 315 by a tidal interaction with another galaxy. By means of *Hubble Space Telescope* (*HST*) images they discovered a knot close to the active nucleus, which they interpreted as a remnant nucleus, proposing a scenario of '. . .an AGN caught in the act of the initiation stage of a tidally induced feeding'.

Finally, Mrk 315 was observed in optical, infrared and radio wavelength domains by Nonino et al. (1998). They confirmed the presence of a secondary nucleus embedded in a chain of faint structures surrounding the active nucleus, and discussed the possible origin of these structures in favour of the merger hypothesis of MacKenty et al. (1994).

Here we present new photometric and spectroscopic data of Mrk 315, which confirm partly the previous findings mentioned above and show for the first time that we are observing the effects of the interaction of two dwarf galaxies with Mrk 315. The paper is organized as follows: the photometric and spectroscopic data are presented in Section 2; the morphology of Mrk 315 is investigated in Section 3; the two-dimensional (2D) spectrophotometric data are analysed in Section 4 with the aim of studying in detail the physical properties of gas in the circumnuclear regions of the galaxy; the stellar and gaseous kinematics is presented and discussed in Section 5; in Section 6 we analyse the environment surrounding Mrk 315 to look for objects physically connected to the galaxy; finally, in Section 7 we discuss the results obtained for each of the features identified in Mrk 315.

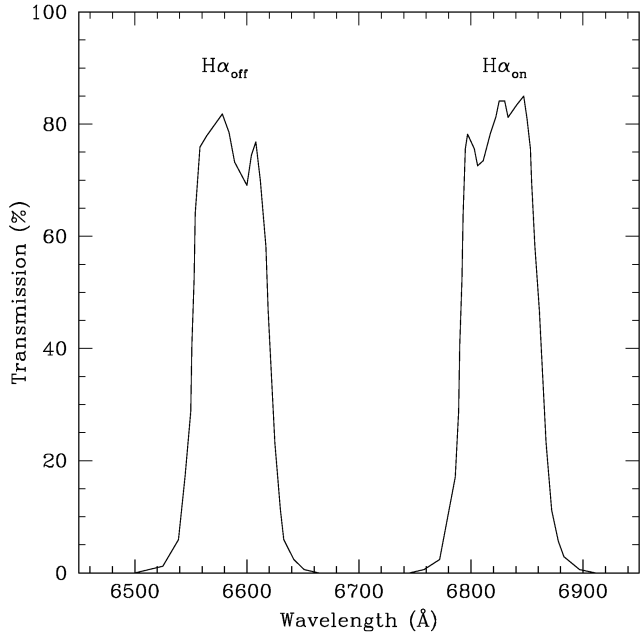

Figure 1. Transmission curves of the VATT narrow-band filters H$\alpha_{\rm on}$ and H$\alpha_{\rm off}$ with central wavelength $\lambda_c = 6830$ and 6580 Å respectively. Both filters have similar width $\Delta\lambda \sim 70$ Å.

2 OBSERVATIONS AND DATA REDUCTION

2.1 Photometry

Broad-band *B* and *R*, and narrow-band Hα ($\lambda_c = 6830$ Å, $\Delta\lambda \sim 70$ Å; H$\alpha_{\rm on}$ hereafter), Hα-continuum ($\lambda_c = 6580$ Å, $\Delta\lambda \sim 70$ Å; H$\alpha_{\rm off}$ hereafter) images were obtained at the 1.8-m Vatican Advanced Technology Telescope (VATT) of the Vatican Observatory (Arizona, USA) in 1998 October, with a 2 k×2 k CCD camera. The transmission curves of the narrow-band filters are plotted in Fig. 1. Middle-band [O III] (filter SED520, $\lambda_c = 5229$ Å, $\Delta\lambda = 310$ Å; [O III]$_{\rm on}$ hereafter), [O III] continuum (filter SED574, $\lambda_c = 5730$ Å, $\Delta\lambda = 160$ Å; [O III]$_{\rm off}$ hereafter), broad-band *V* and $R_{\rm c}$ images were obtained in 2002 August and 2004 September with SCORPIO (Afanasiev & Moiseev 2005), a multimode focal reducer mounted at the 6-m telescope (BTA) of the Special Astrophysical Observatory (SAO-RAS, Russia). See Table 1 for observation details. These images were reduced with IRAF[1] (for VATT images) and with IDL (for the BTA image) in a standard way by subtracting bias and correcting for flat-field variations and cosmic ray events. Also *B*, *V*, $R_{\rm c}$ and I_c images from Chatzichristou (2000), available in NED (NASA Extragalactic Database), were involved in our study. The calibration in the magnitude scale for filters R_c and I_c was obtained by means of a bright star, located 30-arcsec south-east of the galaxy, whose photometry was carried out by Bachev, Strigachev & Dimitrov (2000). Instead, the calibration for filters *B* and *V* was carried out according to published aperture photometry. The six best aperture measurements out of the eight available in the HyperLeda[2] data base have been selected. Finally, for the image obtained with filter [O III]$_{\rm off}$ the calibration was carried out using the *V* band. The zero-point accuracy in any case is better than 0.1 mag.

[1] IRAF is distributed by the National Optical Astronomy Observatories, which are operated by the Association of Universities for Research in Astronomy, Inc., under cooperative agreement with the National Science Foundation.
[2] http://leda.univ-lyon1.fr/

2.2 Panoramic spectroscopy at the 6-m telescope

2.2.1 Integral-field spectrograph MPFS

Mrk 315 was observed in 2000 December and 2003 August with the MultiPupil Fibre Spectrograph (MPFS), the integral-field unit mounted at the primary focus of the 6-m telescope (Afanasiev, Dodonov & Moiseev 2001). The MPFS takes simultaneous spectra from 240 spatial elements (constructed in the shape of square lenses) that form on the sky an array of 16 × 15 elements (in 2000), or from 256 spatial elements (16 × 16 in 2003). The angular size is 1 arcsec element^{-1}. The detector was a TK1024 in 2000 and EEV CCD42-40 (2048 × 2048 pixel) in 2003. A description of the MPFS is available at the SAO RAS web page (http://www.sao.ru/hq/lsfvo/devices.html).

During the first run, the galaxy was observed at low resolution for spectrophotometric purposes, while the second run was addressed to the gas and stellar kinematics investigation, and the galaxy was observed at higher resolution. The log of the MPFS observations is given in Table 2.

The data were reduced using the software developed at the SAO RAS by V. L. Afanasiev and A. V. Moiseev and running in the IDL environment. The primary reduction included bias subtraction, flat-fielding, cosmic ray hits removal, extraction of individual spectra from the CCD frames, and their wavelength calibration using a spectrum of a He–Ne–Ar lamp. Subsequently, we subtracted the night-sky spectrum from those of the galaxy. The spectra of spectrophotometric standard stars were used to convert counts into absolute fluxes.

Table 1. Photometric observations.

Date	T_{exp} (s)	Filter	Seeing (arcsec)	Scale (arcsec pixel^{-1})	FOV (arcmin)	Instr.	Tel.
1998 October 29	1200	B	1.5	0.4	6×6	CCD Camera	VATT
	600	B					
	1200	R					
	600	R					
	1200	Hα_{on}					
	1200	Hα_{off}					
2002 August 30	1800	[O III]$_{on}$	1.6	0.29	5×5	SCORPIO	BTA
	1800	[O III]$_{off}$					
2004 September 08	1320	V	1.6	0.35	6×6	SCORPIO	BTA
	600	R_c	1.5				

Table 2. Spectroscopic observations.

Date	T_{exp} (s)	Sp. range (Å)	Sp. res. (Å)	Disp. (Å pixel^{-1})	Seeing (arcsec)	Instr.	Mode
1994 August 17	1500	4700–5700	2.2	0.8	1.2	ISIS	
2000 December 03	3600	3700–6100	7.5	2.6	1.6	MPFS	
	4800	5000–7400	7.5	2.6	1.6	MPFS	
2003 August 24	14400	4860–6330	4.2	0.75	1.5	MPFS	
2002 November 02	30 × 250	[O III]	1.2	0.54	2.0	SCORPIO	IFP
2002 November 07	900	3700–7300	10.0	1.8	1.5	SCORPIO	Slit

2.2.2 *Scanning Fabry–Perot interferometer*

Mrk 315 was observed in 2003 November with SCORPIO (Afanasiev & Moiseev 2005) in the Fabry–Perot mode. The Queensgate interferometer Fabry–Perot (IFP) ET-50 was used at the 300th interference order (for the redshifted [O III] λ4959 line). The free spectral range between the neighbouring orders (interfringe) was about 16 Å. The detector used was an EEV CCD42-40 operated with 2 × 2 binning for reading-out time saving. The IFP was installed into the parallel beam, inside the focal reducer SCORPIO which provides a field of view (FOV) of ∼6 arcmin and a spatial scale of ∼0.3 arcsec pixel^{-1}. A brief description of this device is also given on the SAO RAS web page (http://www.sao.ru/hq/moisav/scorpio/scorpio.html). In addition, the IFP mode in SCORPIO is described by Moiseev (2002). The log of the IFP observations is presented in Table 2.

To reduce the interferometric observations we used a custom development software (Moiseev 2002), running in the IDL environment. After the primary reduction (bias, flat-field, cosmic hits), we removed the night-sky spectrum, converted the data to the wavelength scale, and prepared them as 'data cubes'. The data cube was smoothed by a Gaussian function with FWHM = 2 pixel in the spectral and spatial domain under the ADHOC[3] package. The spatial resolution after smoothing was about 2.5 arcsec. The velocity fields of the ionized gas, and images in the emission-line [O III] λ4959 were mapped by means of a Gaussian fitting of the emission-line profiles. Moreover, we created the images of the galaxy in the 'red' continuum close to the emission line.

[3] ADHOC software was written by J. Boulesteix (Observatoire de Marseille). See http://www-obs.cnrs.fr/ADHOC/adhoc.html.

2.2.3 *Long-slit spectroscopy*

A long-slit spectrum obtained with ISIS Double Beam Spectrograph at the William Herschel Telescope on 1994 August was extracted from the ING public archive. The grating R600B was used in combination with a 1.5-arcsec slit, at position angle PA = 114°.

We also obtained a long-slit spectrum of a source located ∼1 arcmin south-east of Mrk 315 with SCORPIO in 2002 November. The detector used was the EEV CCD42-40 2048 × 2048 pixel and the slit had a width of 1.2 arcsec.

Data reduction was performed using our IDL-based software for SCORPIO data, and IRAF for ISIS data. We followed the standard procedures applied to long-slit spectra: bias and flat-field correction, 2D wavelength calibration, flux calibration, included atmospheric extinction correction and night-sky background subtraction.

3 MORPHOLOGY

3.1 Isophotal analysis

The morphology of the galaxy was investigated by fitting parametric ellipses to its isophotes in all of the images at our disposal, and fixing the centre at the location of the nucleus. Then, the plots of ellipticity (e) and PA were obtained as a function of the semimajor axis length, expressed in kpc (see Fig. 2). The spatial scale is 0.75 kpc arcsec^{-1} assuming a distance to the galaxy of 153.6 Mpc, directly measured on our spectroscopic data ($V_{sys} = 11517 \pm 9$, see Section 5), and $H_0 = 75$ km s^{-1} Mpc^{-1}. These plots show a first peak in ellipticity between 1 and 2 kpc and a second peak between 3 and 4 kpc. Then, the isophotes have a smooth trend up to the outer regions with ellipticity ranging around $e \sim 0.1$. A slight dip in ellipticity between 8 and 9 kpc corresponds to a change in isophote orientation from

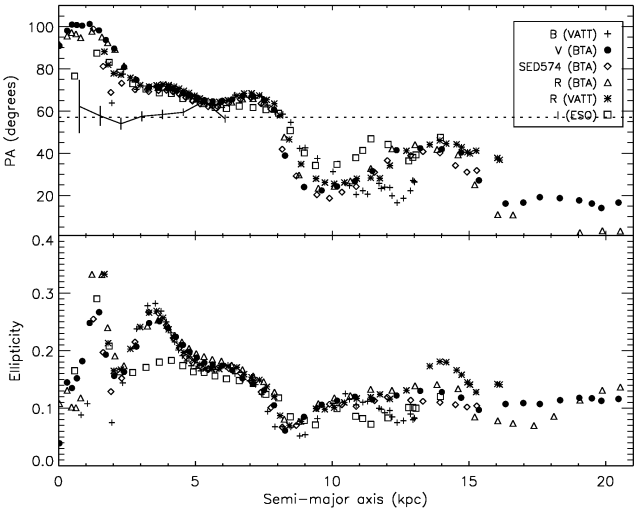

Figure 2. Elliptical isophote parameters from the available images of Mrk 315. In the upper panel the position angle is plotted versus the semi-major axis in kpc. The symbols correspond to different optical bands. The solid line marks the dynamical axis measured on the velocity field of stars (Fig. 14), the dashed line corresponds to the mean value of the dynamical axis (which is accepted as line of nodes). The ellipticity of the isophotes is plotted in the lower panel.

PA $\sim 60°$–$70°$ (between 3 and 8 kpc) to PA $= 15°-40°$ (between 10 and 20 kpc).

3.2 2D decomposition

Mrk 315 is classified in the NED as an elliptical galaxy (type E1), and so the distribution of the surface brightness in its external regions should be described by a spheroidal component. On the other hand, Chatzichristou (2001) argued for an extended external disc in Mrk 315, and stressed that the photometric parameters of the galaxy do not match its morphological type. We tried to decompose the surface brightness distribution by applying 'standard' components: an exponential disc with central brightness μ_d and scalelength r_d and a Sérsic bulge (Sérsic 1968) with effective radius r_{eff}, effective brightness μ_{eff} and power index n varying from 1 to 4. In addition, a point-like source profile was included to account for the presence of the AGN.

The one-dimensional (1D) surface brightness profile and the radial behaviour of the isophotes are too complex to be decomposed in a unique way. A more stable and reliable result could be obtained with the method of the 2D decomposition, which uses the whole bi-dimensional information of the surface brightness distribution (see e.g. Moriondo, Giovanardi & Hunt 1998). We applied the IDL-based software GIDRA, developed at SAO RAS by A.V. Moiseev, and we followed the same iterative method of consecutive comparisons between 1D mean profiles and 2D models, which allowed Moiseev, Valdés & Chavushyan (2004) to study effectively the morphology of double-barred galaxy candidates (see also Sil'chenko & Afanasiev 2000; Sil'chenko, Vlasyuk & Alvarado 2001). The seeing-convolved decomposition was carried out for images in all available bands, and among them we chose deeper BTA data in the filters $[O\,III]_{off}$, V and R_c, because the images from Chatzichristou (2000) reach a lower limit of magnitude, and the VATT images show a significant gradient of the sky background around the galaxy. The limit surface brightness of the BTA broad-band images, corresponding to signal-to-noise (S/N) ratio of 3, is $\mu_V = 26.0\,\mathrm{mag\,arcsec^{-2}}$ and μ_{R_c}=25.7 $\mathrm{mag\,arcsec^{-2}}$.

First, we obtained the azimuthal average of the outer isophotes, whose position angle and ellipticity are expected to correspond to the disc orientation, and we calculated the approximated values of μ_d and r_d by fitting the brightness profile in this disc-dominated region. Then, the 2D model of this exponential disc was subtracted from the original image. The residual image was averaged in annular apertures and the mean profile was fitted by a Sefsic law. Finally, the central peak of brightness was fitted by a 2D Gaussian function, with FWHM similar to the point spread function (PSF) of the image, which corresponds to the active nucleus. The 2D model bulge+core was subtracted from the original image and the cycle was repeated to refine the model.

The model-subtracted images are shown in Fig. 3. In both cases we have detected two characteristic features on these images. First of all, a faint two armed spiral structure is visible in the outer part of the galaxy in the interval $r = 7$–18 arcsec (∼5–14 kpc). Second, the residual image has a significant excess of brightness at $r < 8$–10 arcsec, which originates a 'bump' in the mean profile. The brightness excess can be equally explained with two different orientations of the outer disc, but in this case the kinematic properties of the stars must be involved in our analysis (see Section 7.1). We tried to fit the brightness distribution in this region with an additional inner exponential disc. The resulting parameters of the decomposition are listed in Table 3. The contribution of the components to the total brightness profile are shown in Fig. 3.

3.3 Peculiar features

The brightness excess corresponds to the complex structure surrounding the nucleus, already discovered by MacKenty et al. (1994) and Nonino et al. (1998), and having a quasi-ring shape.

Comparing the Hα continuum-subtracted image with the model subtracted V image (V_{res}), we observe that the emission is extended like this quasi-ring and, even if smoothed, it follows very well its layout, which is therefore characterized by star formation (Fig. 4a). Embedded in this structure is a bright knot (named knot K throughout this paper) marked with 'X' on Fig. 4. This knot is the brightest feature, after the active nucleus, observed on the V_{res} image, but it does not appear as an equally bright Hα source. Conversely, it is well evident in the I-band *HST* image, published by MacKenty et al. (1994), proving its prevailing stellar nature. In fact this knot is the supposed secondary nucleus of the merger hypothesis claimed by these authors.

The [O III] continuum-subtracted image shows a strongly different distribution of the higher ionization gas, which seems only weakly to follow the quasi-ring (Fig. 4b). Of course this is not unexpected, because [O III] emission is usually weak in regions, where thermal ionization by star formation dominates. A prominent feature radially extended from the nucleus up to ∼7 kpc does not correspond to any other structure, suggesting the idea of gas directly ionized by the active nucleus. Moreover, it is interesting to point out that the putative secondary nucleus has no evident, or maybe very weak, counterpart in [O III] emission.

Further, low-brightness structures at S/N ∼ 3–5 are visible in the deep V and R_c images obtained at BTA (Fig. 5). We observe a sort of trail apparently non-coplanar to the disc of the galaxy and wounded around it, and a plume located south-west. At least two stellar shells can be identified ∼15 kpc north and ∼30 kpc north-west of the Galactic disc. Such shells are similar to those discovered in the merger galaxy Mrk 298 (Radovich et al. 2005). In addition,

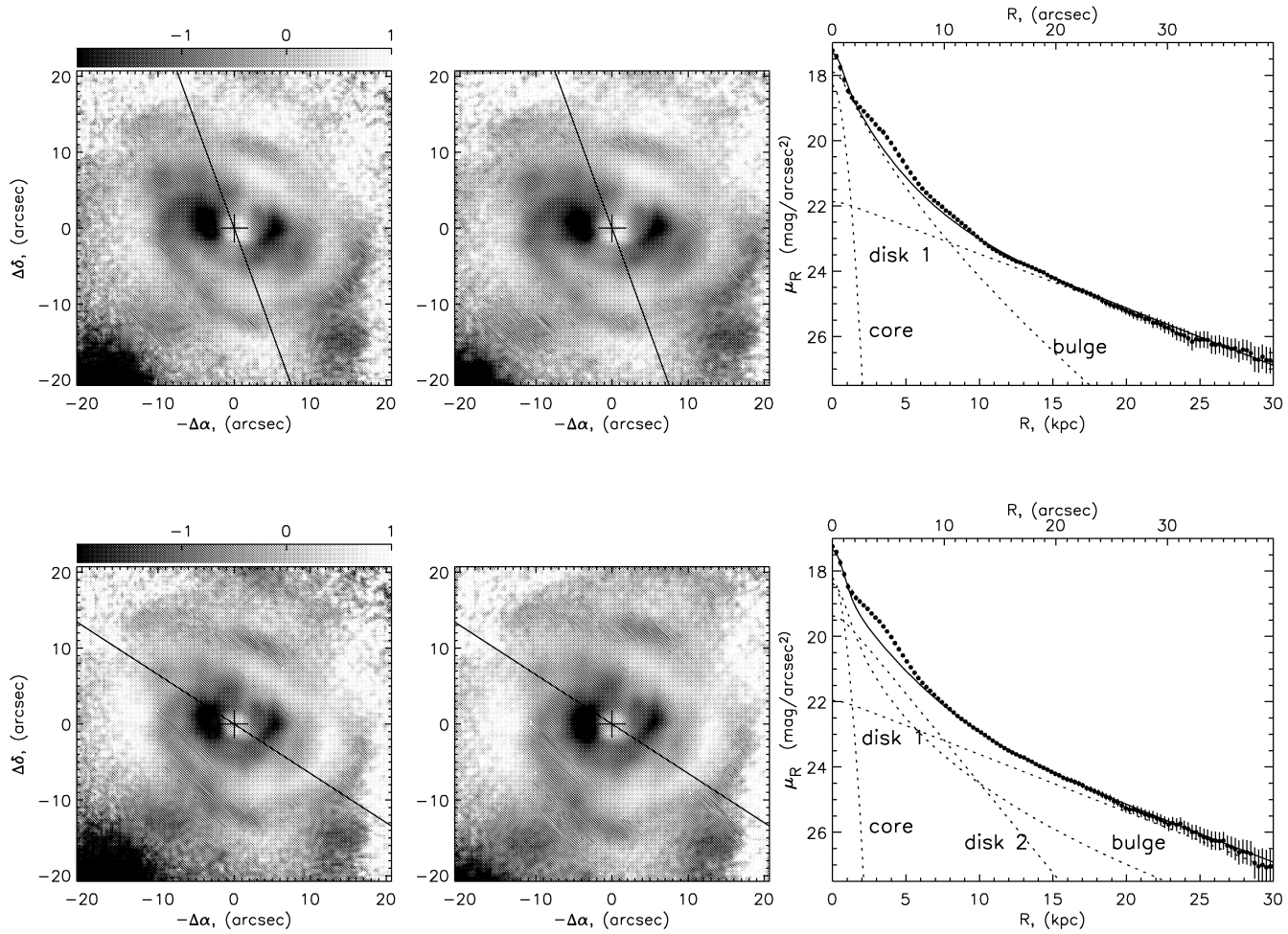

Figure 3. 2D decomposition of the surface brightness distribution in the R_c band. The top row shows the results of a single disc model with PA = PA_{out}. Here the left-hand panel shows the residuals (smoothed) after the model subtraction from the original image in the sky plane, the middle panel is the residual after the deprojection onto the galactic plane. The scale is in magnitudes, the cross marks the photometric centre and the solid line indicates the direction of the line of nodes. The right-hand panel presents the mean profile averaged in annular ellipses. The solid line is the averaged model profile, and the dashed lines are the averaged profiles of the photometric components convolved with seeing. The bottom row is the same, but for two discs model with PA = PA_{dyn}.

Table 3. Parameters of the 2D decomposition of the brightness distribution.

Band	Bulge			Outer disc		Inner disc		Lum. ratio
	μ_{eff} (mag)	r_e (kpc)	n	μ_{d1} (mag)	r_{d1} (kpc)	μ_{d2} (mag)	r_{d2} (kpc)	L_B/L_D
[O III]$_{off}$	20.82 ± 0.33	2.01 ± 0.14	2.0 ± 0.3	22.35 ± 0.04	6.99 ± 0.07	20.06 ± 0.22	2.05 ± 0.08	0.62 ± 0.13
V	21.70 ± 0.18	2.55 ± 0.13	3.0 ± 0.3	22.79 ± 0.05	7.07 ± 0.10	19.58 ± 0.10	1.90 ± 0.04	0.56 ± 0.12
R_c	21.09 ± 0.21	2.49 ± 0.15	3.0 ± 0.3	21.85 ± 0.05	6.16 ± 0.08	19.03 ± 0.06	1.98 ± 0.03	0.52 ± 0.13
V	19.69 ± 0.07	3.05 ± 0.30	1.7 ± 0.4	23.10 ± 0.05	7.60 ± 0.11			2.67 ± 0.35
R_c	19.75 ± 0.10	2.35 ± 0.04	1.5 ± 0.2	21.77 ± 0.04	6.31 ± 0.05			2.47 ± 0.29

two filaments are laid in the surroundings of Mrk 315. The first one (F1 hereafter), already identified by MacKenty (1986), extends up to ∼70 kpc from the central regions of the galaxy at PA ∼ 145°. The second one (F2 hereafter) seems to begin ∼75 kpc north-west of the galaxy. Then, it crosses F1 in projection, extends at PA ∼ 120° toward the north-east side of the galaxy, where it turns to PA ∼ 0°, and finally ends at the location of an extended source ∼45 kpc south-east of Mrk 315. The total projected extension of F2 is ∼140 kpc.

4 SPECTROPHOTOMETRIC DATA ANALYSIS

The low-resolution spectra were analysed with IRAF tasks. A correction for Galactic absorption, $A(V) = 0.68$, was applied and the atmospheric absorption band at 6860–6920 Å was removed by means of the flux-calibrated spectrum of the standard star.

Several emission lines are present in Mrk 315 spectra. To perform a more precise measurement of their fluxes, these lines were

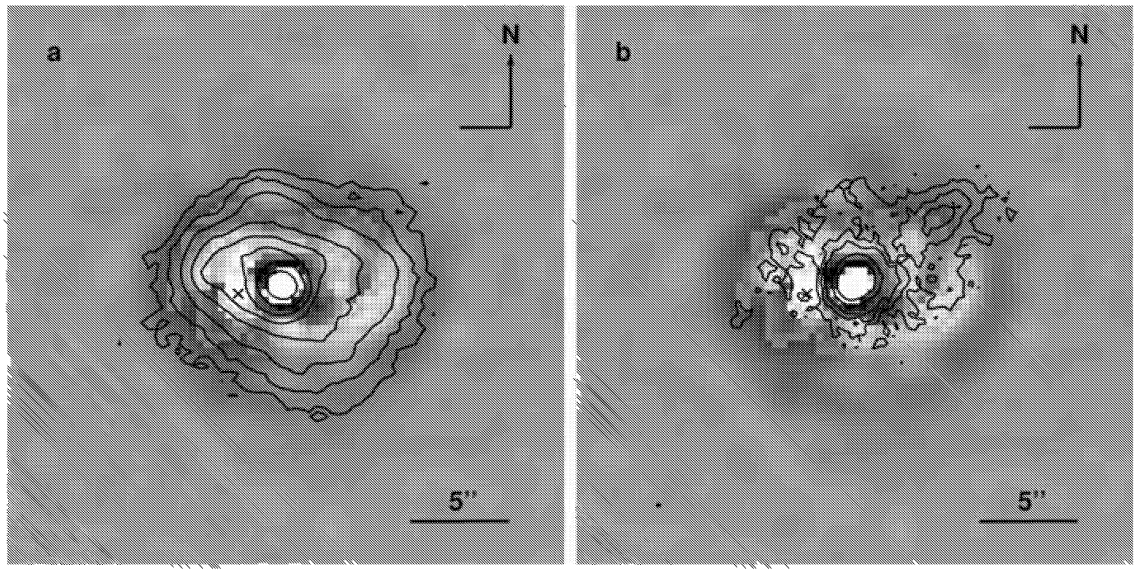

Figure 4. The quasi-ring structure. Contours are the isointensities of the non-calibrated Hα (*a*) and [O III] (*b*) continuum-subtracted images of Mrk 315. The cross marks the position of the knot identified by MacKenty et al. (1994) as a possible secondary nucleus.

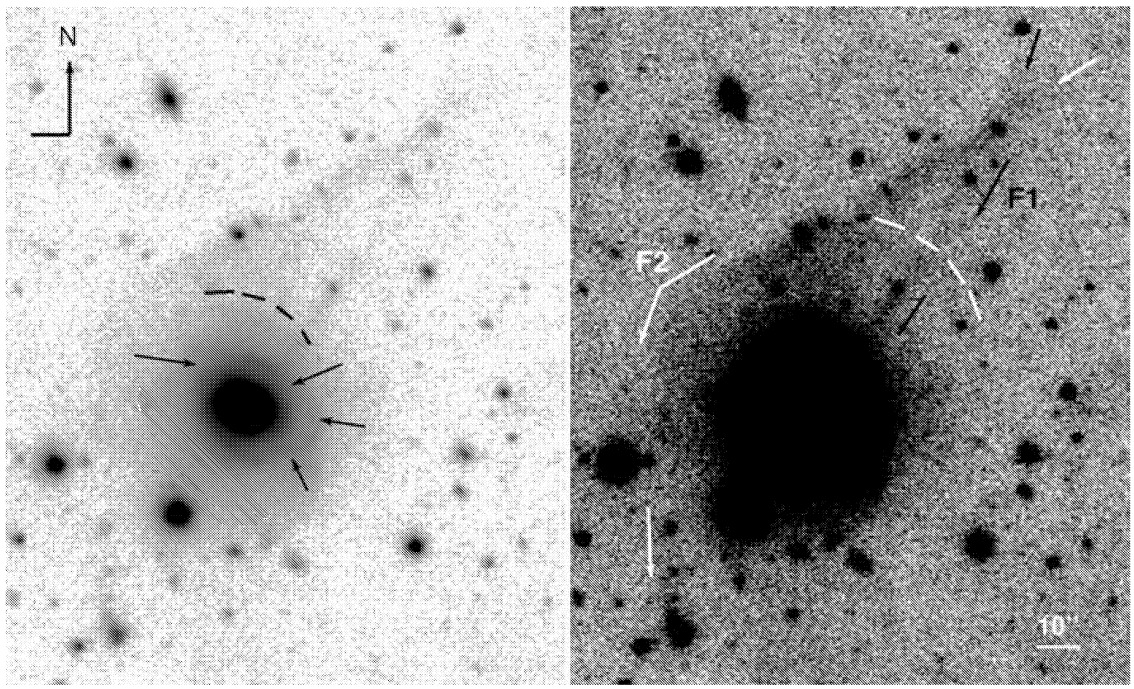

Figure 5. The *V* image of Mrk 315 with different grey-scale levels to emphasize the weak inner (left-hand panel) and outer (right-hand panel) features. In the left-hand panel, black arrows indicate the position of the wounding trail, while the dashed line indicates the location of the inner stellar shell. In the right-hand panel, black arrows follow the wake toward the secondary nucleus (named F1 in the text), while white arrows indicate the wake toward the south-east extended source (named F2 in the text). The white dashed line indicates the position of the outer shell. The scale bar corresponds to 7.5 kpc at the distance of the galaxy.

corrected for the underlying stellar contribution. An IRAF task made by us on the basis of the insights given by Ho, Filippenko & Sargent (1993b) allows to subtract the spectrum of a template early-type galaxy after having conveniently rescaled its continuum and diluted its absorption features (see Ciroi et al. 2003, for a more extensive discussion about this step).

A first reconstruction of the galaxy image in the FOV of the spectrograph was done convolving each spectrum with the transmission curve of a typical Johnson *V* filter. This image together with narrow-band images obtained integrating in a small wavelength range around Hα and [O III] λ5007 allowed to locate the position of the nucleus in the brightest pixel. This position does not coincide with that shown by a similarly reconstructed image in [O II] λ3727, because of the atmospheric refraction effect. To solve the problem we calculated the correction function to be applied to each image before any comparison. This was done simply producing

several narrow-band continuum images covering both spectral ranges and measuring the centroid of the galaxy in each image with a bi-dimensional Gaussian fitting. Finally the centroid positions were interpolated separately as a function of wavelengths.

As Mrk 315 is an intermediate-type Seyfert galaxy, its nuclear spectrum shows permitted lines with composite profiles: a narrow component emitted by the narrow-line region (NLR) and a broad component emitted by the broad-line region (BLR). Given its subparsec size the BLR can be considered as a point-like source, therefore its emission will not be limited to the nuclear spectrum, but distributed in the surrounding regions depending on the seeing during the observations. In order to obtain spectra with only NLR emission lines, we applied the following procedure. First, a hand-made PSF was reproduced in the FOV of MPFS with a bi-dimensional normalized Gaussian function centred on the brightest pixel (in the Hα reconstructed map), where the BLR should be located, and with a FWHM similar to the seeing value. Then, the spectrum of the brightest pixel was measured. A deblending of the Hα+[N II] $\lambda\lambda$6548, 6583 profile by means of an iterative multi-Gaussian fitting procedure involving four components, Hα broad (Hα_b), Hα narrow (Hα_n), [N II] λ6548 and [N II] λ6583, allowed us to build a spectrum showing only Hα_b. This spectrum was replicated to cover the entire FOV, and the 240 Hα_b lines were rescaled to obtain the spatial distribution of the BLR emission in Hα. This was done by multiplying each of them for the scaling factor given by the pixel intensity of the PSF at the corresponding location on the FOV. Finally these spectra were subtracted from those containing both BLR and NLR emission lines.

Two parameters were fine tuned to better remove the broad component: the FWHM of the PSF and its position within the pixel where the active nucleus is located. Obviously a bi-dimensional Gaussian is only an approximation of the real PSF and moreover the low-spatial resolution (1 arcsec) implies that even an off-centring of 0.2 pixel can distribute the flux in a significantly different way. These are the reasons why we could not fix these two parameters a priori. The same steps were applied to Hβ.

After having removed the broad emission lines, the spectra of Mrk 315 were measured. An IRAF task made by us and based on a recursive application of NGAUSSFIT allowed to interactively fit each emission line with Gaussian functions, and obtain tables with fundamental parameters, as position, flux, FWHM, amplitude and equivalent width. These tables can be quickly used to reconstruct maps of the 16×15 resolution elements for whatever of these parameters. Relative errors were also calculated by estimating the rms of the continuum close to each emission line. In most of the spectra, the fluxes of the brightest lines have errors below 30 per cent (Table 4).

4.1 Emission-line ratios

We have reconstructed maps of the most important emission lines visible in the spectra of Mrk 315, i.e. [O II]λ3727, [O III]λ4363, He IIλ4686, Hβ, [O III]λ5007, [O I]λ6300, Hα, [N II]λ6583 and [S II]λ6716 + 31 (also named [S II]λ6724 throughout this paper). These maps, grouped in Fig. 6, show the spatial distribution of the ionized gas. Maps of Hβ and Hα lines have a smoothed shape, where structures are not easy to be distinguished because of the low-spatial resolution. Nevertheless, a significant improvement is reached by overlapping the contours of the V_{res} image (Fig. 7a). These contours helped us to identify integral-field spectra belonging to specific regions. In particular we defined the nucleus (N), three regions of the quasi-ring structure (A1, A2, A3), numbered counter-clockwise from south-west to north-east, and finally the knot (K) located 2.5-arcsec east of the nucleus.

A similar procedure was used for the [O III] map, whose shape is well in agreement with the contours of the [O III] continuum-subtracted image (Fig. 7b). On this map we have isolated other two regions, one radially extended from the nucleus and north-west oriented (J1), the other smaller and fainter, located ∼6 arcsec east of the nucleus (J2). Finally, [O I] and [S II] maps clearly show a secondary bright emission region identified with the knot K. In Fig. 8 we plotted the integrated spectra of these identified regions.

Then we have calculated the emission-line ratio maps on the basis of the diagnostic diagrams of (Veilleux & Osterbrock 1987, VO hereafter), i.e. [O III]/Hβ, [N II]/Hα, [O I]/Hα and [S II]/Hα. These ratios are useful to study the ionization of gas and identify the kind of ionizing source. As done before, each ratio map was compared with a contour ([O III] continuum-subtracted image, or V_{res} image) to make the analysis clearer (Fig. 9). [N II]/Hα and [O I]/Hα ratios show peaked values at the location of the knot K. This is visible also in the [S II]/Hα map, where a larger structure extends clockwise from K towards the west in the outer part of A3. High values of the [S II]/Hα ratio are also located south of A1. The [O III]/Hβ map shows two loci where the gas is highly ionized, except for the nucleus: J2 and the outer regions of J1.

We have also reconstructed the map of the [O II]/[O III] emission-line ratio (Fig. 10), which is abundance independent and a good indicator of the ionization degree. Unlike the pairs of emission lines used by the VO diagnostic diagrams, which are close in wavelength so that their ratios are almost unaffected by dust extinction, the [O II]/[O III] ratio must be reddening corrected. Therefore we have first calculated the observed Hα/Hβ ratios and applied a theoretical Balmer decrement of 2.86 to all emission regions but the nucleus N, where a 3.1 was used following the suggestions by Osterbrock (1989). As the extinction law we used the one given by Cardelli, Clayton & Mathis (1989). The map of the visual absorption A_V (Fig. 11, right) shows clearly that the major extinction is distributed in a region including N, K and J2 with values ranging from 2 to 3 mag (light grey). Lower values ($A_V \sim$ 1–1.5) are typical of A1, A2 and A3, while in J1 the extinction is negligible.

The map of the reddening corrected [O II]/[O III] ratios shows two zones (dark grey) located on the nucleus N and on J1, where the [O III] is dominant ([O II]/[O III] < 1) and the ionization is mainly produced by the AGN. The [O II] is stronger than [O III] ([O II]/[O III] >3–10) roughly in correspondence of the other regions A1, A2, A3 and K (light grey), thus indicating the prevailing thermal origin of the ionization sources.

Table 4. Flux errors of the measured emission lines. Columns (1)–(6) show the percentage of spectra whose relative flux errors are below the values given in column (7).

[O II] 3727	[O III] 4363	He II 4686	Hβ	[O III] 5007	[O I] 6300	Hα	[N II] 6583	[S II] 6724	$\Delta I/I$
42	5	0	65	61	10	73	65	57	<0.10
80	24	12	82	82	53	88	83	73	<0.20
96	38	53	94	89	74	94	92	83	<0.30

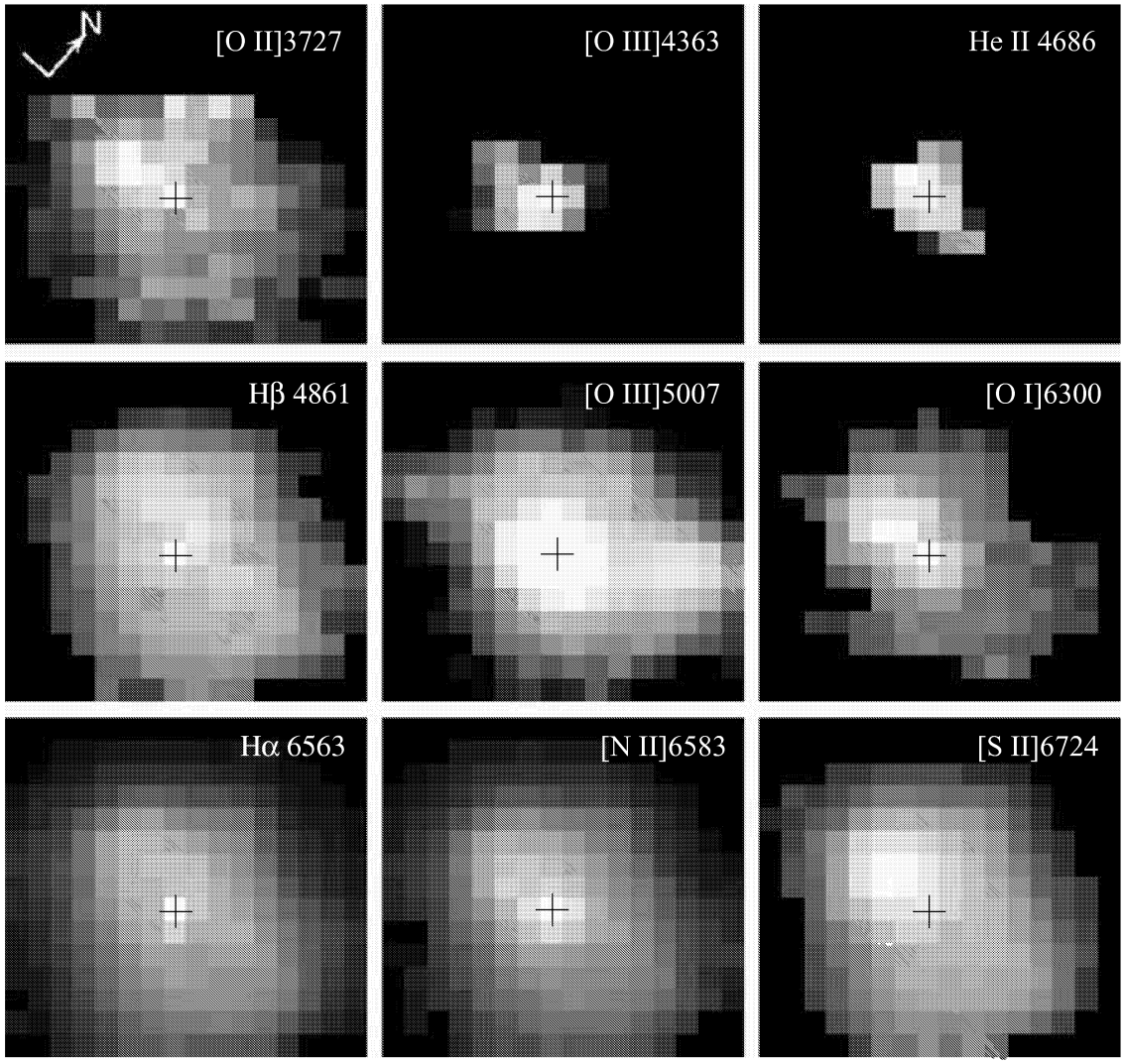

Figure 6. Reconstructed maps of the galaxy for different emission lines in the FOV of the spectrograph (16×15 arcsec). Each pixel corresponds to 1×1 arcsec. The arrow indicates north, the cross marks the position of the nucleus.

Finally, the map of the electron density (n_e) distribution, given by the [S II]6716/6731 ratio (Fig. 11, left), shows the highest values ($\sim 10^3$ cm^{-3}) where also the extinction is higher, while it assumes values in the range 100–300 cm^{-3} north of the nucleus, including A3, and even less than 100 cm^{-3} in A1 and A2.

To carry out a more detailed analysis we plotted the emission-line ratios [O III]/Hβ versus [N II]/Hα, [O I]/Hα and [S II]/Hα respectively, (Figs 12a–c) according to the VO diagrams. We added the empirical borderlines, which separate AGN from H II regions (solid line), and AGN from LINER or supernova remnants (SNRs; dashed line), or in other words define the ranges of ratios for which non-thermal, thermal or shock ionization dominates. An inspection of the diagrams suggests that the observed ratios are consistent with the structure identified in the image analysis (see Section 3). In particular spectra belonging to N (open circles) fall in the AGN zone, although three of them are close to the AGN/LINER borderline. Interestingly, all spectra around the central one (the brightest pixel in e.g. Hβ, Hα or [N II] maps of Fig. 6) where the active nucleus is expected to be located, show higher [N II], [O I] and [S II] to Hα values. On the contrary, spectra of K (filled circles) fall in the LINER/SNR zone and show a lower ionization degree ([O III] $\approx$ Hβ). Thanks to the relatively good seeing, N and K spectral properties are well discriminated even if they are close to each other. The easiest and maybe more corrected interpretation is that the gas in region K is dominated by shock effects. Nevertheless, we cannot rule out the possibility that K itself is an active secondary nucleus, namely a LINER. A1 and A3 have most of their line ratios typical of H II regions (open squares and crosses respectively), while A1 has some close to the AGN/H II borderline and A3 shows some values of [O I] and [S II] to Hα falling in the LINER/SNR zone. These last points are located among regions N, K and A3 and their line ratios strongly indicate that the gas is compressed and shock ionization occurs. Region A2 has line ratios mostly falling in the H II region zone (filled squares), but two of them are close to the AGN/H II borderline. These two spectra of A2 are just those near the nucleus N, and therefore are probably 'polluted' by AGN radiation. Indeed it was shown by Radovich, Hasinger & Rafanelli (1998) that an increasing contribution to the AGN ionization by star-forming regions pushes the emission-line ratios from the AGN toward the H II zone. J1 has five spectra in common with A2 and one in common with A1. In agreement with what we said before about J1 and the [O III]/Hβ map, the inner parts of J1 (skeletal triangles) are characterized by

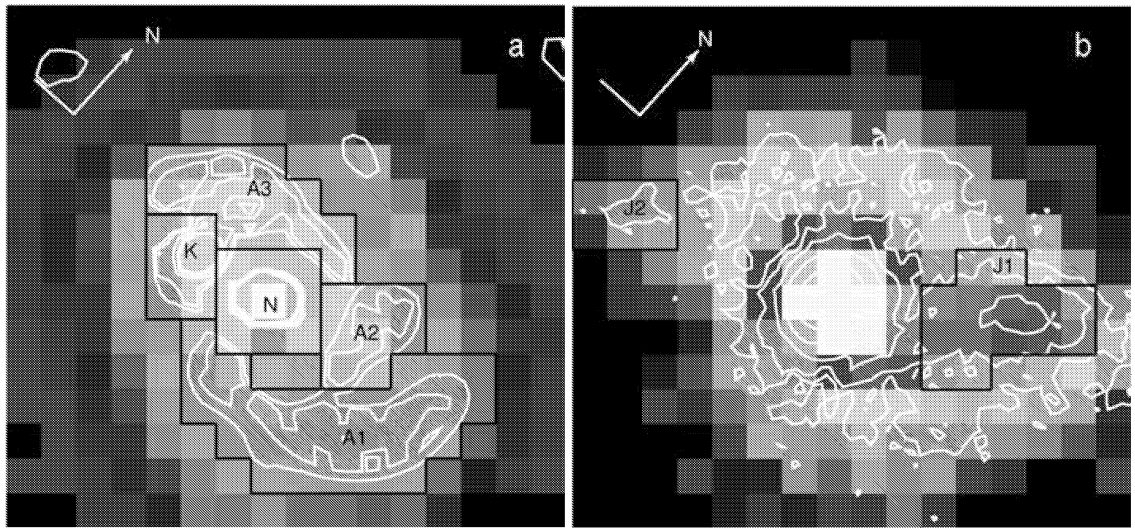

Figure 7. (*a*) Hα integral-field map. The white contours are the isointensities of the $V_{\rm res}$ image. The black lines define the selected regions N, K, A1, A2 and A3. (*b*) [O III] integral-field map. The white contours are the isointensities of the [O III] continuum-subtracted image. The black lines define the selected regions J1 and J2.

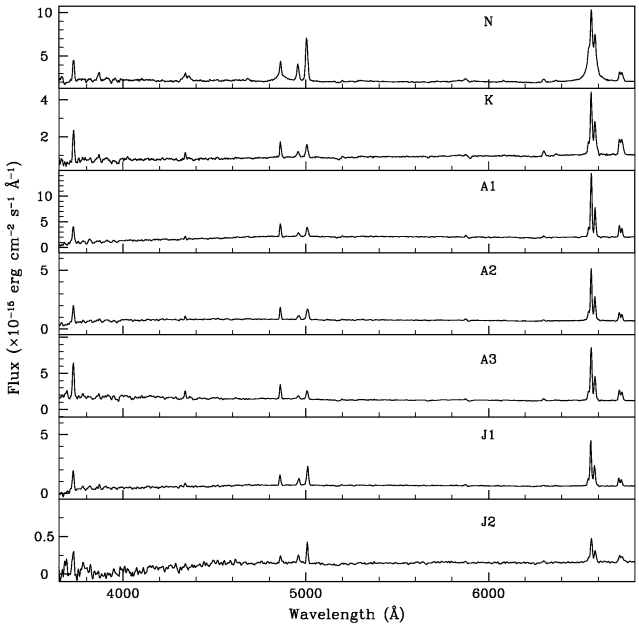

Figure 8. The integrated spectra of the regions identified in Fig. 7.

lower ionization, while the outer parts fall in the AGN zone. This is not unexpected because the overlap between J1 and A2 makes lower the emission-line ratio [O III]/Hβ because Hβ is strong in star-forming regions. The outer parts of J1 (>7 arcsec) are reached by AGN radiation, and so J1 can be considered an ionization cone. It is likely that J1 and A2 overlap only in projection on the sky, but are not coplanar. The other cone could be located in region J2 (open stars), whose spectra have also AGN-like properties. Its small extension and relatively faintness could be caused by the fact that we are observing it through the disc of the galaxy.

The remaining emission regions have line ratios mostly filling the H II zone in all VO diagrams, while few points have AGN properties, in particular those around J1, therefore characterized by diffuse AGN radiation, and finally others fall in the LINER/SNR zone. A more careful identification of these last points, carried out by reconstructing the map of their positions within the field of view, reveals that they form a ring around the identified regions. This ring is made mostly by regions whose spectra have LINER/SNR properties only in the [S II]/Hα diagram, while few regions are present in two diagnostics or in all the three. In addition two adjacent regions not connected to the ring have a LINER/SNR identification in all the three plots, and are located among N, A1 and A2. The shape and displacement of these regions suggests that shocks caused by gas compression around the inner quasi-ring structure could be at the origin of their emission-line ratios. Nevertheless a single plot based indication makes this hypothesis not completely convincing, because the regions whose spectra show higher values of [S II]/Hα ratio could simply have an overabundance of [S II], even if in this case the ring-like distribution of these regions remains unexplained.

4.2 Star formation rate and energy budget

We have used the Hα emission to estimate the star formation rate (SFR) in the field of view of integral-field data. The Hα reddening corrected fluxes were first converted into luminosities, then the total luminosities of the portion of galaxy observed with MPFS, and of each region identified on the Hα emission-line map, were calculated. Finally, we applied the formula by Kennicutt (1998) $\mathrm{SFR(M_\odot\ yr^{-1})} = 7.9 \times 10^{-42} L_{\rm H\alpha}$. In Table 5 we list these values, together with the surface density of the SFR in $\mathrm{M_\odot\ yr^{-1}\ pc^{-2}}$ units. The total $L_{\rm H\alpha}$ includes also the nuclear contribution, which is clearly AGN dominated and therefore the SFR value is overestimated. Removing $L_{\rm H\alpha}(N)$, which accounts for about 22 per cent of the total $L_{\rm H\alpha}$, we obtain SFR $\sim 35\ \mathrm{M_\odot\ yr^{-1}}$ and $\Sigma_{\rm SFR} \sim 4.36 \times 10^{-7}\ \mathrm{M_\odot\ yr^{-1}\ pc^{-2}}$.

For consistence with these results, we tried to estimate SFR by using other two indicators, the infrared and radio emissions. We used the *IRAS* data of Mrk 315 extracted from the Point Source Catalogue, and in particular the 60-μm flux, $S_{60} = 1.505$ Jy. Then, we followed the suggestions given by Chapman et al. (2000), based on Rowan-Robinson et al. (1997), who made use of the 60-μm luminosity to estimate the total far-infrared (FIR) emission within the range

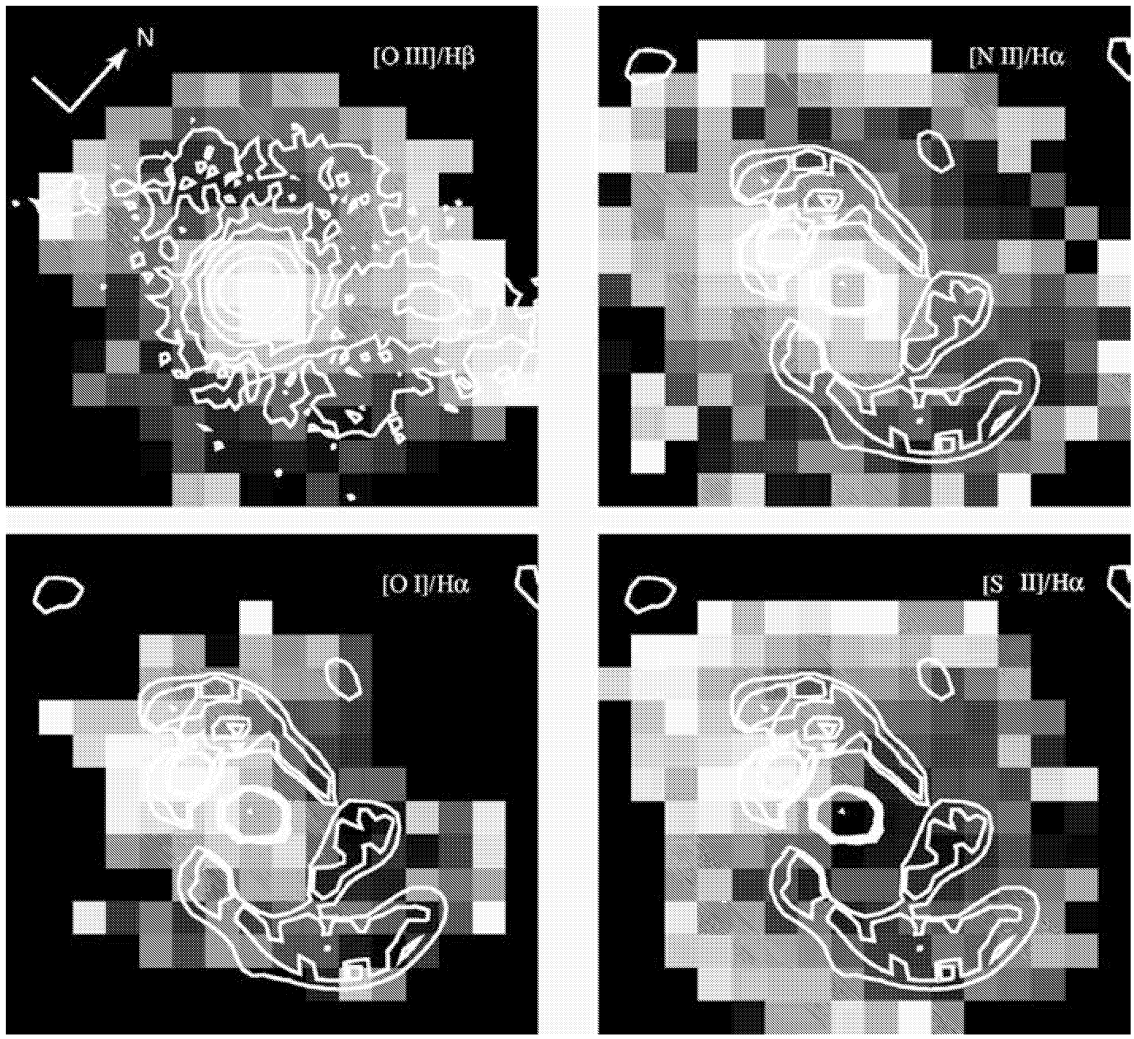

Figure 9. Integral-field maps of the emission-line ratios used in diagnostic diagrams. The contours of the $V_{\rm res}$ image are overlaid for all maps, but the [O III]/Hβ where the contours of the [O III] continuum-subtracted image are used. The brightest pixels have ratios with the highest values.

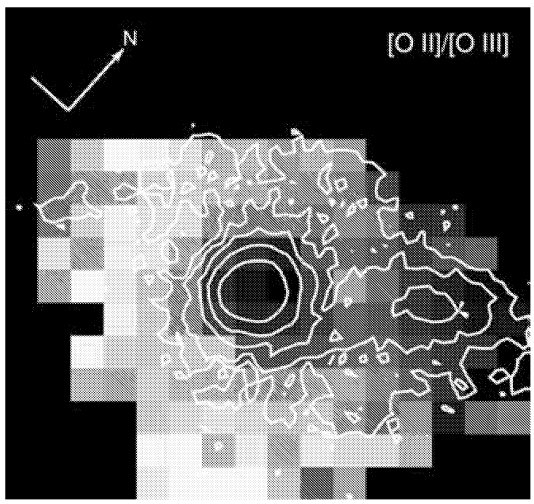

Figure 10. Map of the reddening corrected [O II]/[O III] ratio. The brightest pixels have the ratios with the highest values. The contours of the [O III] continuum-subtracted image are overlaid.

1–1000 μm, $L_{\rm FIR} \sim 1.7 \times L_{60}$ erg s^{-1}, and converted into the SFR with the formula: SFR(M$_\odot$ yr^{-1}) = $L_{\rm FIR}/2.2 \times 10^9$ L$_\odot$. We obtained the following values, $L_{\rm FIR}$(1–1000 μm) = 3.32×10^{44} erg s^{-1} and $SFR \sim 39$ M$_\odot$ yr^{-1}. Also in this case, the total FIR emission includes the AGN contribution, therefore this value of SFR should be considered as an upper limit.

The radio emission value at 1.425 GHz was taken from Nonino et al. (1998), who measured the total flux and the contribution from the nucleus and the knot separately. We removed the nuclear emission obtaining $S_{20} = 19$ mJy, and luminosity $L_{20} = 5.38 \times 10^{22}$ W Hz^{-1}. This value was then converted into SFR using the formula given by Bell (2003), and obtaining ∼30 M$_\odot$ yr^{-1}, in good agreement with the SFRs found by using Hα and FIR emission.

From the radio luminosity we also calculated the supernova (SN) rate, because at 1.425 GHz the radio emission is usually dominated by non-thermal radiation (synchrotron) produced by electrons accelerated by SNRs and explosions. To obtain the non-thermal luminosity $L_{\rm NT}$, we followed the assumption by Condon & Yin (1990) and Bell (2003) that the thermal radio fraction at 1.425 GHz is about 10 per cent. Then, we applied the relation $L_{\rm NT}$(W Hz^{-1}) ∼ $1.3 \times 10^{23}(\nu/1\ {\rm GHz})^{-\alpha} \nu_{\rm SN}$ (yr^{-1}), given by Condon & Yin (1990), and

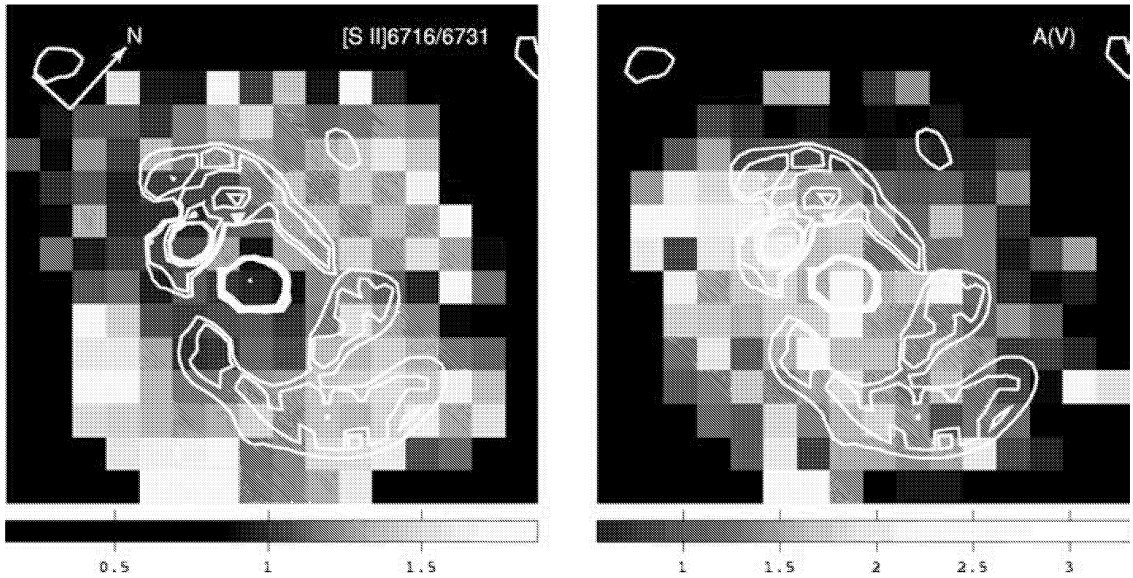

Figure 11. Left: integral-field map of the [S II] doublet ratio, which indicates the distribution of the electron density (n_e) over the field of view. Dark grey pixels correspond to the highest values of n_e. Right: the map of the internal reddening A(V) obtained from the Hα/Hβ ratios. The brightest pixels are those with the highest extinction. The white contours of the V_{res} image are overlaid onto both panels.

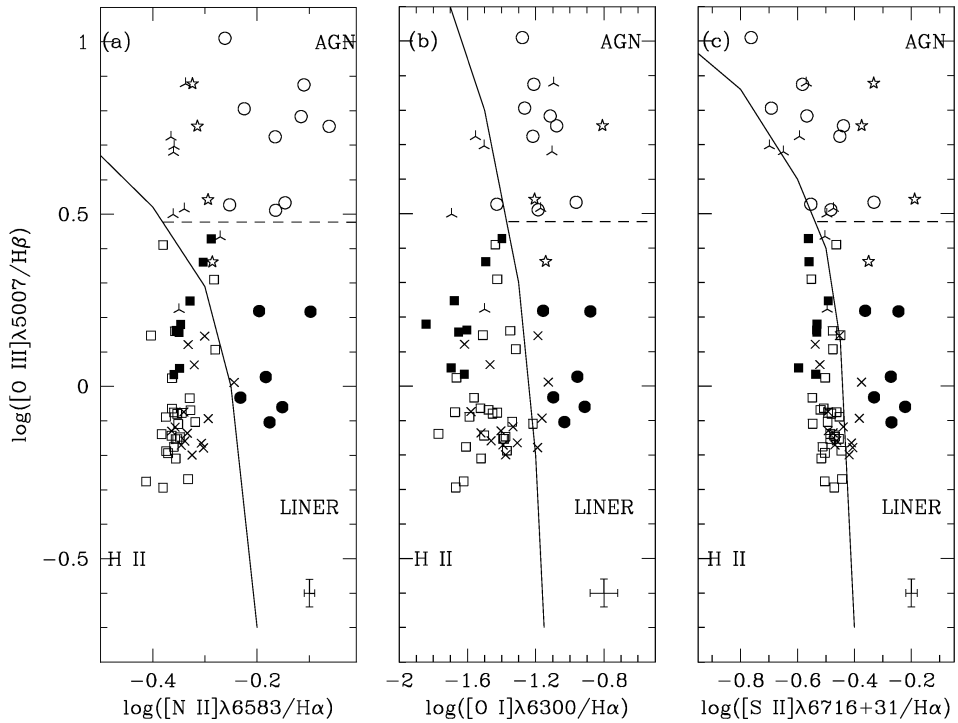

Figure 12. Veilleux & Osterbrock (1987) diagnostic diagram showing the emission-line ratios from the regions selected in Fig. 7: N (open circles), K (filled circles), A1 (open squares), A2 (filled squares), A3 (crosses), J1 (skeletal triangles) and J2 (open stars). The solid and the dashed lines separate the zones where thermal, non-thermal and shock ionization occurs. The error bars indicate the typical errors for the diagnostic ratios of these regions.

we adopted the spectral index $\alpha = 0.9$ for the overall galaxy (Nonino et al. 1998). The SN rate (ν_{SN}) is about 0.5 yr^{-1}, a value much higher than that expected in normal spiral galaxies, 1 SN/100 yr per 10^{10} L$_\odot$ (B) (see e.g. van den Bergh & Tammann 1991), but consistent with the rates observed in starburst galaxies, which are typically in the range 0.1–1.0 yr^{-1} (Smith, Lonsdale & Lonsdale 1998; Mannucci et al. 2003; Neff, Ulvestad & Teng 2004). The equally high SFR is in agreement with observations of starburst galaxies, as in the local Universe mildly obscured and UV luminous starbursts show rates of 5–50 M$_\odot$ yr^{-1} (Heckman et al. 2005).

As the VO diagrams indicate that the J1 region, especially its outer part, is highly ionized, it is interesting to evaluate whether the nuclear radiation can sustain this observed high ionization degree. To carry out this test, we have first isolated a region of 3×2 arcsec,

Table 5. Hα luminosities and SFRs.

Region	$L_{H\alpha}$ (10^{42} erg s^{-1})	SFR ($M_\odot$ yr^{-1})	Σ_{SFR} ($M_\odot$ yr^{-1}pc^{-2})
N	1.30	...	...
K	0.50	3.9	1.13×10^{-6}
A1	1.14	9.0	5.79×10^{-7}
A2	0.47	3.7	8.10×10^{-7}
A3	0.84	6.6	8.19×10^{-7}
Total	5.84	46	5.32×10^{-7}

located ∼6 arcsec north-west of the nucleus, within J1 and showing a spectrum dominated by AGN excitation according to the diagnostic diagrams. In the approximation that the AGN is the only source producing the Hα photons observed in this region, we converted its total Hα luminosity into the number of ionizing photons $Q_{ion} = 7.3 \times 10^{11} L_{H\alpha}$ (Osterbrock 1989). Then we corrected this number for the effect of the geometrical dilution of the nuclear radiation flowing through the solid angle Ω subtended by the region, $Q_{nuc} = (4\pi/\Omega) \times Q_{ion} \sim 3 \times 10^{54}$ photons s^{-1}.

Now we use this rough estimate of the number of ionizing photons emitted by the source, to calculate the expected ionization parameter $U = Q_{nuc}/(4\pi\, r^2\, N_H c)$ at the distance of the region. Assuming $r \sim 4.6$ kpc and $N_H \sim 10^2$ cm^{-3} (obtained from the [S II]6716/6731 ratio), we obtain $\log U \sim -3.4$. This value does not agree with observed line ratios. A simple comparison with published photoionization models (see e.g. Ho, Shields & Filippenko 1993a; Ho et al. 1993b), indicates that this expected ionization parameter is typical of a low ionization degree. Indeed, the [O II]/[O III] emission-line ratio ∼0.4–0.5 (reddening corrected), observed both in the nucleus and in the region should correspond to a value of $\log U \sim -2.5$ (Penston et al. 1990; Komossa & Schulz 1997). In the end, the nuclear ionizing radiation alone seems not enough to produce the high-excitation levels detected in J1, especially in its outer parts. Another source of high-energy photons must be present, like hot stars, or more likely shock waves. A similar result was obtained by MacKenty (1986), who followed a different approach.

5 KINEMATICS

The kinematics of Mrk 315 was investigated essentially by means of the integral-field MPFS and Fabry–Perot data.

5.1 Fabry–Perot data

The kinematics of the highly ionized gas was studied in detail through the spectral analysis of the [O III] emission line. The high resolution of the Fabry–Perot data allowed to clearly separate two distinct components in the emission-line profile: a first component belonging to the disc of the galaxy and showing a pattern of almost circular rotation with velocities ranging from 11 350 and 11 750 km s^{-1}, and a second 'redder' component corresponding to the previously mentioned J1 and J2 regions, and characterized by high-velocity gas radially moving toward the outskirts of the galaxy. The difference to the systemic velocity is ∼+500 km s^{-1}. In addition, the first kinematic component shows a clear nuclear outflow with $V \sim 11\,480$ km s^{-1} (Fig. 13).

We remark that the disc circular rotation seen in [O III] agrees with the circular rotation observed in Hα and in the velocity field of stars (see next section).

The analysis of the long-slit spectrum, even if at lower resolution, showed the same two kinematic components both in [O III] and in Hβ. We fitted separately these components, and then we compared the velocity curves with the Fabry–Perot data extracted at the same PA of the slit, obtaining a good agreement.

We compared also our results with those published by Wilson (1988), who found the two kinematic components in [O III], one characterized by rotational motions, and the other extended from the nucleus toward north and north-west with an unclear kinematical structure. Unlike Wilson (1988), we observe clearly the blueward and redward components both in [O III] and in Hβ. Moreover, we observe a larger splitting of the two kinematic components than Wilson (1988), maybe because of an higher spectral resolution which allowed us to obtain more precise measurements of the line profiles.

5.2 MPFS data

The low-resolution MPFS spectra were used to derive the overall kinematics of both low- and high-ionization gas within the FOV. First, the wavelength positions of Hα emission lines were measured by means of Gaussian fittings and then converted into heliocentric velocities. Later we constructed the maps of the line-of-sight velocity fields of the brightest emission lines. The absolute accuracy of the velocity measurements, evaluated from the air-glow emission-line wavelengths, was about 10–15 km s^{-1}. A continuum map was also obtained by adding the fluxes in the spectral ranges free from emission lines (5600–5900 Å).

Velocity maps show a deviation from circular rotation in oxygen ([O I], [O II], [O III]) and sulphur ([S II]) lines. In particular, in [O II] we can see a sudden increase of velocity with $\Delta V \sim +300$ km s^{-1}, where the knot K is located. A sudden decrease of velocity ($\Delta V \sim -200$ km s^{-1}) in [O III] confirms the outflow already shown by Fabry–Perot and long-slit data.

The kinematics of the stellar component in Mrk 315 was studied by means of the high-resolution MPFS data. The line-of-sight velocity and dispersion velocity fields were constructed. We used the 'classic' cross-correlation method adapted for working with MPFS spectra (Moiseev 2002). The region 5050–6050 Å containing numerous stellar absorption features (Mg I, Fe I, Na I etc.) was analysed. As a template for cross-correlation the spectra of the twilight sky, observed in the same night as the galaxy, were used. The estimated errors were ∼10 and 10–20 km s^{-1} for the velocity and velocity dispersion, respectively. The line-of-sight velocity distribution (LOSVD) of the stars in the central region of the galaxy shows two clearly peaked structures, with a separation of about 600 km s^{-1}. By means of a double-Gaussian fit of the LOSVD we have constructed maps of line-of-sight velocity and velocity dispersion for both components. The results are shown in Fig. 14. Both components have velocity fields with a pattern corresponding to circular rotation of inclined discs. The centre of rotation of the 'blue' LOSVD component coincides with the photometric nucleus of Mrk 315, and the centre of rotation of the 'red' LOSVD component coincides with the position of the knot K, within the limits of 1 arcsec. In the following we will identify the 'blue' component as the main galaxy, and the second component as the 'satellite'.

The analysis of the velocity fields of the main galaxy and the satellite was carried out by means of the method of the 'tilted-rings' model (Begeman 1989). More details about this method, in connection to the MPFS velocity fields, are given in Moiseev et al. (2004). The average parameters of the orientation of the rotated discs are listed in Table 6. The relatively high error in the system

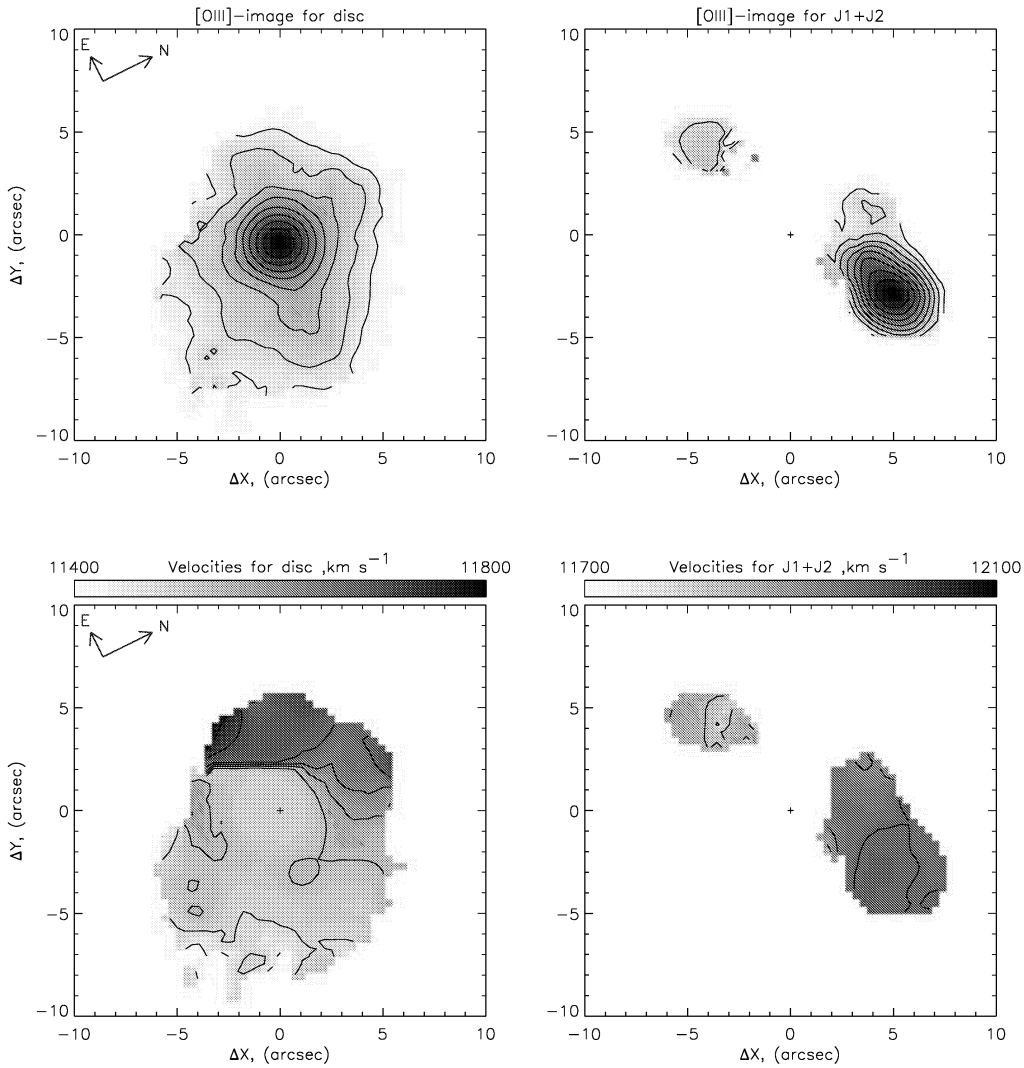

Figure 13. The velocity field of gas obtained with Fabry–Perot observations in the emission line [O III]. Two kinematic components can be separately studied. The left-hand panel shows the rotation of the galaxy with the additional nuclear outflow. The right-hand panel shows the high-velocity gas corresponding to the J1 and J2 regions.

velocity of the satellite is caused by an observed smooth change of $V_{\rm sys}$ with radius. Most likely, it is connected to the influence of the tidal interaction on the dynamics of the satellite. Indeed, in the azimuthal Fourier decomposition of the velocity field there is a systematic change of the harmonic with $m = 1$, which is interpreted in the frame of the circular rotation as a radial trend of the systemic velocity.

In Fig. 14 the curves of the circular rotation for each of the galaxies, and the azimuthally averaged radial distribution of the velocity dispersion are also shown. We observe a rather small velocity dispersion of the stars in Mrk 315, in comparison with a large amplitude of the rotation curve, which does not reach a plateau within the limit of 5 kpc from the centre. The ratio of the maximum velocity of rotation to the maximum velocity dispersion, $V_{\rm max}/\sigma \sim 3.5$, extremely exceeds the mean value which is usually observed in the bulges of the early-type galaxies (0.1–1.5, Kormendy 1982). Moreover, there are no significant deviations of line-of-sight velocity of the galaxy from the pure circular rotation. Therefore, the stellar kinematics in Mrk 315 support the idea that we are observing rotation of stars in a disc, instead of a dynamically 'hot' bulge.

In the centre a sharp decrease of the velocity dispersion of stars is also observed, with values less than 50–70 km s^{-1}, which cannot be measured with our spectral resolution. Recently Wozniak et al. (2003) explained such drops in the radial velocity dispersion distribution of a number of Seyfert galaxies, within the framework of the self-consistent dynamic model. According to these authors, this effect is caused by stars which were born in the centre from a dynamically cold gas having a smaller velocity dispersion, than the older star population. Wozniak's model has been constructed for galaxies with bars, but in our opinion it can be applied also to Mrk 315, where the gas in the centre can be connected to tidal effects, instead of a secular evolution of a bar. Also, as mentioned in Section 7.1, the bar could have existed here, but been dissolved by interaction.

Thus, our analysis of stellar kinematics in Mrk 315 clearly distinguishes two independently rotating subsystems separated in systemic velocity by more than ∼600 km s^{-1}. Estimating the masses of these stellar systems within the FOV by means of the virial approximation $R \times V^2$, we obtain that the satellite has a mass about 10 times lower than the mass of the main galaxy. Therefore, our data demonstrate that the knot K is the debris of a nucleated dwarf

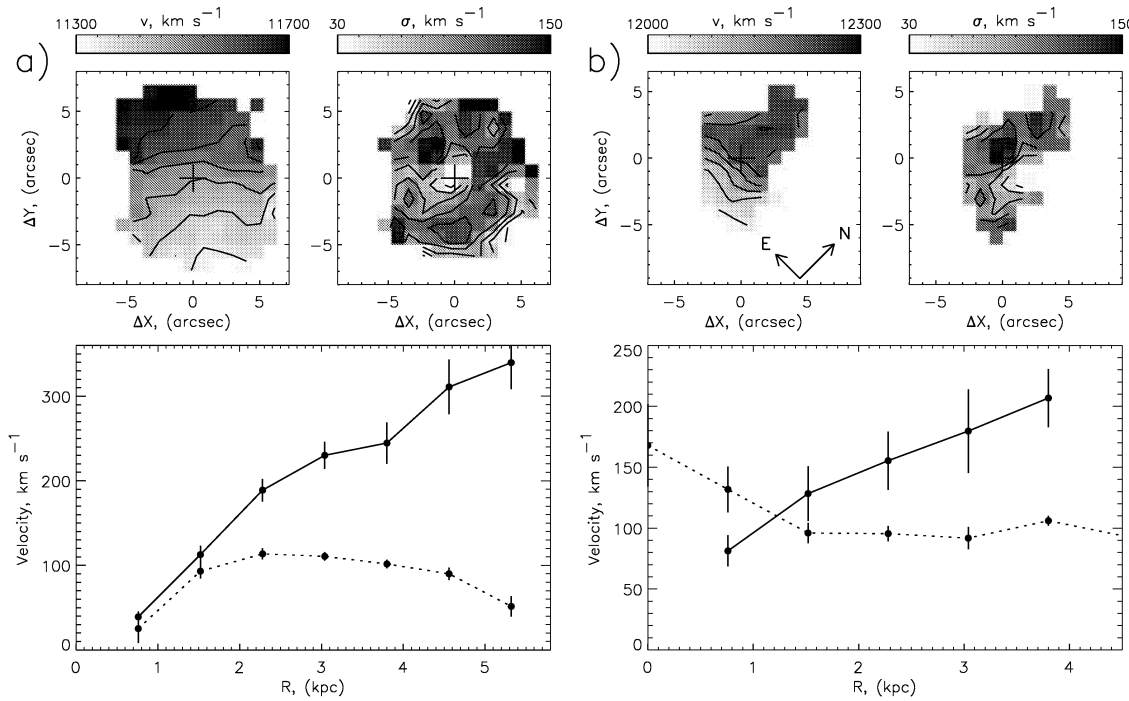

Figure 14. Stellar kinematics obtained with MPFS data. (a) The 'main galaxy' component: the line-of-sight velocity field and the map of the velocity dispersion are reproduced in the upper panels. The cross marks the dynamical centre. The rotation curve (solid line) and the average radial distribution of the line-of-sight velocity dispersion (dotted line) are plotted in the lower panel. (b) The same for the secondary component, named 'knot K' in the text.

Table 6. Kinematic parameters of the stellar components.

Name	V_{sys}(Hel) (km s^{-1})	PA_{dyn} (°)	i (°)
Main galaxy	11517 ± 9	57 ± 4	34 ± 3
Satellite	12164 ± 22	2 ± 6	35 ± 10

galaxy companion of Mrk 315, which experienced a minor merger episode.

The stellar velocity in knot K and the gas velocity in J1 and J2 are not in fully agreement with stellar velocities of the satellite, but at least within 150–200 km s^{-1}. They are not kinematically connected to the main galaxy, but there could be a relationship between them. As the mass of K is largely smaller than the mass of the main galaxy, the collision should not change significantly the morphology of the main galaxy, but it can compress the gas and trigger the process of fuelling of the active nucleus. Nevertheless, it is unlikely that such a small galaxy can throw away gas at the observed velocity along J1.

6 THE ENVIRONMENT

To study the environment of Mrk 315, we applied the criteria proposed by Schmitt (2001) to consider a candidate companion as physically bound to the active galaxy: (1) the distance to the main galaxy must be smaller than five times the diameter of that galaxy; (2) the difference in brightness between them must be $|\Delta m| \leqslant 3$ mag; (3) the difference in radial velocities must be $|\Delta v| \leqslant 1000$ km s^{-1}. On the DSS2 red image (Fig. 15a) we found a galaxy located east of Mrk 315 just at the distance of about five diameters (∼3.4 arcmin), which satisfy also the brightness criterion ($|\Delta m| \sim 1.2$ mag). This galaxy is catalogued in NED as 2MASX J23041747+2237302, but unfortunately no information is available about its redshift. Therefore, according to these criteria Mrk 315 can be considered a moderately isolated galaxy.

Its overall morphology does not show strong distortions, bright tidal tails or similar structures, which lead immediately to conclude that this galaxy experienced past episodes of gravitational interactions. Nevertheless, our analysis confirmed the presence of a secondary nucleus very close to the active nucleus. This secondary nucleus originated likely by a dwarf satellite which sank into the main galaxy.

Moreover, inspecting carefully the [O III] continuum-subtracted image, we discovered an emitting source located ∼1 arcmin south-east of Mrk 315 (Fig. 15b). We measured the aperture magnitude V and R_c of the active galaxy and this source, obtaining $V = 14.60 \pm 0.09$, $R_c = 13.92 \pm 0.07$ (aperture diameter=100 arcsec) and $V = 20.0 \pm 0.3$, $R_c = 19.7 \pm 0.2$, respectively. Clearly, the south-east source does not fit the brightness criterium. Nevertheless, it is associated to a bright extended H I cloud (Simkin & MacKenty 2001). This cloud could be an integral part of the outer regions of the main galaxy, which is H I deficient at velocities where the gas is ionized, that is in the filament F1 or in the regions of starburst activity near the nucleus. We obtained a low-resolution slit spectrum of this source with SCORPIO (Fig. 16). This spectrum shows prominent emission lines at a velocity ∼+200 km s^{-1} relative to V_{sys} of Mrk 315, and a clear stellar continuum. Therefore this source, which has also a tidal-disturbed shape visible on the broad-band images, is a dwarf satellite of the active galaxy.

We conclude that the criteria applied to evaluate the isolation of a galaxy are often biased toward bright companions, and therefore are useless in the case of an environment populated by dwarf galaxies.

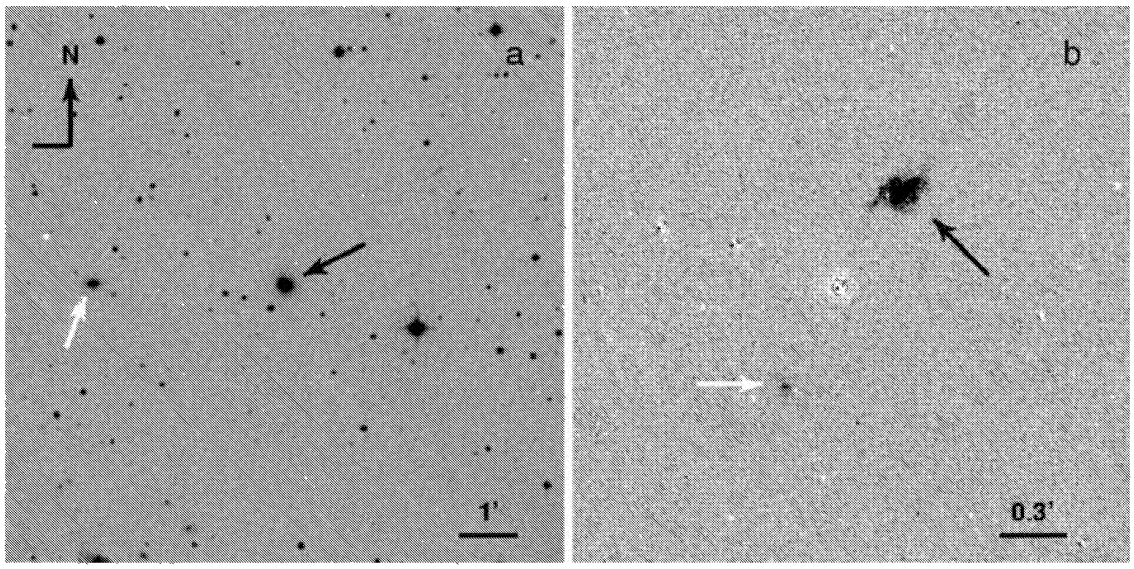

Figure 15. The POSS2-red field around Mrk 315 (a). The black and white arrows indicate the positions of Mrk 315 and the nearest brightest galaxy 2MASX J23041747+2237302. The [O III] continuum-subtracted image of Mrk 315 (black arrow) and the location of the dwarf emission-line galaxy (white arrow).

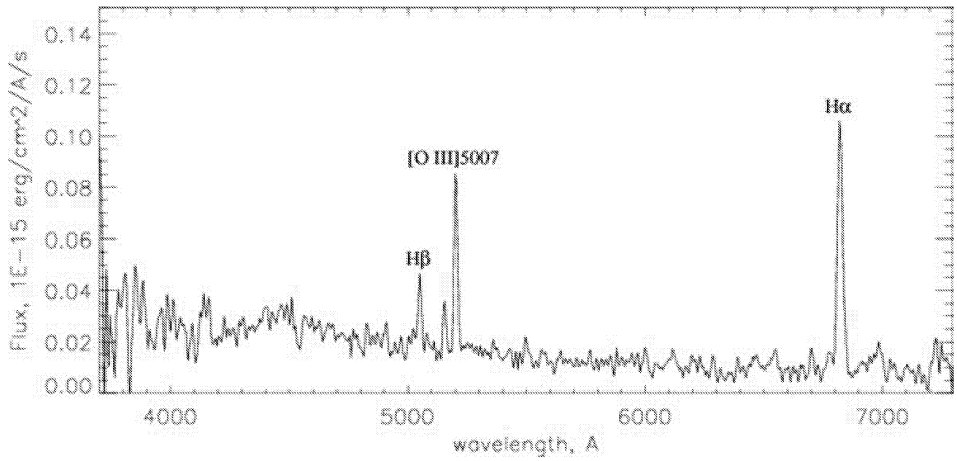

Figure 16. The low-resolution spectrum of the dwarf emission-line galaxy identified in [O III] with SCORPIO.

During the last two decades many authors have studied the environment of active galaxies, mainly using a statistical approach and applying different isolation criteria to define a companion galaxy. For many reasons, as for example the crucial point of the control sample selection, they reached contradictory results (see e.g. Schmitt 2001, and references therein). Therefore, to date a solid evidence that nuclear activity is induced by the environment does not exist. On the contrary less attention has been paid to dwarf satellites in relation to minor merger events. Recently, on the basis of the Sloan Digital Sky Survey (SDSS) Early Data Release (EDR) Miller et al. (2003) observed a high fraction of AGNs (∼40 per cent) in their sample of nearby galaxies. They explained their result with either an AGN duty cycle longer than previous estimates by other authors, or with several bursts of the nucleus driven by mergers. As they did not observe any dependence on environment of their AGN sample, they rejected the second hypothesis. Again, this analysis is limited to bright galaxies [$M(r^*) < -20$], and does not take into account the possible presence of dwarf satellites. Indeed, converting our magnitudes into the SDSS photometric system (Fukugita et al. 1996), we obtained $M(r') = -21.8$ for Mrk 315 and $M(r') = -16.1$ for the south-east companion.

De Robertis et al. (1998) and Taniguchi (1999) suggested that 'minor mergers' between a gas-rich galaxy and a satellite companion may play a significant role in triggering activity in Seyfert nuclei. Indeed the minor merger seems to be the favourite mechanism for several reasons. First of all there is evidence that most spiral galaxies have dwarf satellites (Zaritsky et al. 1997) and therefore minor merger events are expected to occur several times during the lifetime of a galaxy. Second, numerical simulations (see e.g. Hernquist & Mihos 1995) showed that minor mergers can drive a sufficient amount of gas from the host galaxy into its central kiloparsec in a relatively rapid time-scale (<1 Gyr). Third, minor mergers do not cause strong deformations of the host morphology, and indeed most Seyfert galaxies do not appear significantly different from non-active galaxies. In fact, as reported by Taniguchi (1999), the minor merger time-scale could be long enough to smear its

relics, therefore most of the advanced mergers would be observed as ordinary-looking isolated galaxies.

7 DISCUSSION

Mrk 315 has been investigated by means of both new imaging and spectroscopic data. The galaxy has several peculiar features in spite of the fact that it appears like a rather 'normal' early-type spiral. We discuss separately these features in the following subsections.

7.1 Redshift

We have compared the heliocentric systemic velocity of Mrk 315, $V_{\rm sys} = 11517 \pm 9$ km s^{-1}, obtained with the spectroscopy of the stellar component, with the values given in the literature. By inspecting carefully the previously published papers about this galaxy, we found a redshift of 11 827 km s^{-1} given by Sargent (1970) and Huchra & Sargent (1973) based on measurements of optical emission lines. We remark that this value is referred to the Galactic centre, and when converted to heliocentric reference frame, it becomes ∼11 640 km s^{-1}. The discrepancy with our redshift could be caused by the use of the emission lines. In fact, the nuclear spectrum shows hydrogen Balmer lines with asymmetric profiles caused by their broad components, which make them useless for measuring systemic velocity, and high-ionization lines affected by the nuclear outflow. A value of 11 827 km s^{-1}, coincidentally identical to the one given above, but in this case referred to heliocentric reference frame, was obtained by Mirabel & Wilson (1984) with H I observations. The large difference with optical measurements could be caused by the low spatial resolution of their data (3.3 arcmin). In fact, this beam includes the south-east dwarf galaxy, which is an H I source much stronger than Mrk 315 (with a flux about nine times higher). This appears clear in higher resolution H I data recently published by Simkin & MacKenty (2001), and showing well-separated H I sources with velocities of ∼11 800 and ∼11 670 km s^{-1} for the south-east dwarf and the main galaxy, respectively. Finally, the weak H I cloud relative to Mrk 315 appears not perfectly centred on its nucleus and extended toward the north-west. This could have been caused by gravitational interaction effects, and could justify the discrepancy between the radio data and our systemic velocity measurement.

7.2 Morphology

At first sight the morphology of Mrk 315 does not show signs of past or ongoing interaction. Apart from the peak of ellipticity close to the nucleus and caused by the presence of the knot, named K throughout this paper, the isophotes of the galaxy are almost regular in their ellipticity. However, in all analysed images after the subtraction of the 2D surface brightness models, two faint spiral arms are visible in the external parts. The presence of these spiral arms is likely to cause the observed change of the position angle of the external isophotes.

The 2D decomposition process of the surface brightness distribution allowed us to give the correct interpretation of the morphological parameters observed in the galaxy. At the beginning we have considered two possible choices for the orientation of the disc component in Mrk 315: (1) $\mathrm{PA_d} \equiv \mathrm{PA_{out}} \sim 20^\circ$ and $i_{\rm d} \equiv i_{\rm out} \sim 30^\circ$, obtained from the parameters of the external elliptical isophotes between 10 and 20 kpc; (2) $\mathrm{PA_d} \equiv \mathrm{PA_{dyn}} = 57^\circ$ and $i_{\rm d} \equiv i_{\rm dyn} = 34^\circ$, measured on the velocity field of stars between 1 and 6 kpc;

In the first case (Fig. 3 top) the residual brightness is negative (oversubtracted) at PA $\sim 0^\circ$ and positive at PA $\sim 60^\circ$–70°, where the knot K is located, and resemble that of an elongated bar-like feature in the galactic plane. But if this is a real bar, then the non-circular motions of stars must shift the $\mathrm{PA_{dyn}}$ in the gas/stellar velocity field from the PA of the line-of-nodes towards the opposite direction relative to the bar major axis (see discussion and references in Moiseev et al. 2004). However, $\mathrm{PA_{dyn}} = 57^\circ$, so it is turned to the same direction of the bar major axis, as in case of disc kinematics. Therefore the bar-like structure is an artifact. Moreover, the morphological type of the galaxy is not consistent with the model result. On one hand, the bulge-to-disc (B/D) luminosity ratio is $L_{\rm B}/L_{\rm D} \sim 2.5$ as in a E-S0 galaxy (see Simien & de Vaucouleurs 1986). On the other hand, the bulge follows an almost exponential profile (index $n \sim 1.5$), which is rather strange for an early-type galaxy (see e.g. Moriondo et al. 1998).

In contrast, the morphological structure becomes clear if we consider the second choice for the disc orientation, that is by applying our kinematic measurements. First, the B/D ratio becomes $L_{\rm B}/L_{\rm D} \sim 0.5$–$0.6$, which corresponds to a Sab type according to Simien & de Vaucouleurs (1986), and the Sérsic index $n \sim 3$ is in a good agreement with this early morphological type. Secondly, there is no more a displacement between the stellar velocity field and the orientation of the disc. Thirdly, the map of the residual brightness deprojected onto the galactic plane (see Fig. 3 bottom) shows a symmetric ring-like feature within 6 arcsec, in agreement with the disc-like kinematics of this region, which remains even when an outer secondary exponential disc is taken into account. This feature matches the star-forming quasi-ring analysed in Section 4. Finally, the presence of an inner disc allows us to explain the relatively small value of the velocity dispersion of stars within a radius of 5 kpc (see Section 5.3). Because this inner disc has a surface brightness greater or equal to that of the bulge (between 2 and 8 kpc), the dynamically cold component influences significantly the line-of-sight velocity dispersion.

In this frame, the significant twist of the outer isophotes can be explained as a warp of the outer disc. Substituting the parameters of the outer isophotes $\mathrm{PA_{out}} = 20^\circ$–$30^\circ$ and $i_{\rm out} = 30^\circ$ in the equation (2) by Moiseev et al. (2004), we predict that the angle between the inner (<8–10 kpc) and outer (15–20 kpc) parts of the galaxy is $\Delta i \sim 15$–20°. This result is consistent with a galaxy which experienced an interaction process (see e.g. Reshetnikov & Combes 1999), and therefore the presence of a warped disc is not surprising.

Over recent years a multicomponent structure of the Galactic disc has been found in numerous galaxies, e.g. NGC 615 (Sil'chenko et al. 2001) or the intriguing case of NGC 7217 (Sil'chenko & Afanasiev 2000) with three exponential discs increasing their radial scales outward. In addition, Pizzella et al. (2002) showed nuclear discs embedded in the bulges of three early-type galaxies. Erwin et al. (2003) found luminous inner discs inside bar regions of two barred galaxies, NGC 2787 and 3945, and in the last one the inner disc is ten times more luminous than the bulge. Moiseev et al. (2004) also detected inner discs within a 1-kpc sized region of seven barred galaxies. To date the origin of these inner discs is explained with a 'secular evolution' of the Galactic disc, or a redistribution of the gaseous matter provoked by a bar, or a moderate gravitational interaction with other galaxies (see discussion in Sil'chenko et al. 2001). Mrk 315 has no bar, but we found that it experienced interaction with two dwarf satellites. In addition our model-subtracted images show a ring in the central region (with the same scale of the inner disc) with two bright peaks. The eastern peak is a satellite sank into the galaxy (knot K), but the western peak belongs to the

galactic plane, and therefore the azimuthal brightness distribution of the ring is non-uniform. This situation is analogue to the results of numerical simulations of the flight of a small satellite through a barred galaxy performed by Athanassoula, Puerari & Bosma (1997). Their fig. 19 shows that the impact destroys the bar and form a ring on a time-scale $\sim 5 \times 10^7$ yr after the impact. Therefore, we suggest that the inner disc component in Mrk 315 could be the debris of a bar.

7.3 Quasi-ring

In analogy with Nonino et al. (1998), who applied the method of isophotal fitting with ellipses to make a model of the galaxy and subtract it from the original image to show fine structures, we were able to enhance an internal quasi-ring structure, embedded in the bright diffuse emission of the galaxy, and in which we have identified three main regions (labelled A1, A2 and A3). This structure, whose existence was already indicated by MacKenty et al. (1994) as a ring, is similar to that shown in fig. 1 of the Nonino et al. (1998) paper, who called it a 'chain' of knots surrounding the Seyfert nucleus. We stress that we do not observe the 'emission dip' found by these authors at PA $\sim 225^\circ$, which should be located roughly in the middle of A1.

This quasi-ring is characterized by diffuse Hα emission, without any evident condensation, while [O III] is very faint suggesting the thermal origin of the ionizing sources. Indeed, integral-field spectra of regions A1, A2 and A3 exhibit the typical emission lines and line ratios observed in H II and star-forming regions: low values of [N II]/Hα ($<$0.6), [O III]/Hβ ($<$3) and high values of [O II]/[O III] ($>$1). This result is in agreement with Wilson (1988), who measured [O III]/Hβ = 0.4–1.0 and claimed for hot star photoionized gas outside the nucleus, where the kinematics is dominated by circular motions.

The total Hα luminosity, corrected for internal reddening, and then converted into SFRs clearly indicates that Mrk 315 is a starburst galaxy. Our result is solid because we have cross-checked the high SFR value found using Hα with infrared and radio emission, which gave substantial agreement. It is remarkable that Nonino et al. (1998) claimed an overall SFR of $\sim 1\ M_\odot\ yr^{-1}$ on the basis of *IRAS* data taken from Mazzarella, Bothun & Boroson (1991). We tried to investigate the reason for this large difference by repeating the calculations made by these authors, and we found a possible oversight in their FIR luminosity value, which is lower by a factor of $\sim$10. Indeed Nonino et al. (1998) are not able to explain why a such low FIR luminosity, and therefore SFR, can be related to a high value of the SN rate given by the radio emission. Moreover they used both 60- and 100-μm *IRAS* fluxes to obtain FIR emission, but while at 60 μm the source is well defined and its emission easily measurable, at 100 μm the galaxy is embedded in large and bright structures which prevent a reliable estimate of the background level and therefore of the source flux. This is probably why the value at 100 μm published by Mazzarella et al. (1991) is an upper limit ($\leqslant$0.76 Jy), and it is largely distant to the flux given in the Faint Source Catalogue ($\leqslant$4.526 Jy).

Through the analysis of the gaseous and stellar kinematics of this structure, and more in general of the galaxy, we found out that the velocity fields are made by independent kinematical components. In particular, the main component of the galaxy is characterized by almost pure circular rotation, with the dynamic centre located at the photometric nucleus of Mrk 315. This is a major difference between our results and those presented by MacKenty et al. (1994), and later mentioned by Nonino et al. (1998), who located the kinematic centre 6-arcsec north-west of the nucleus. In our opinion these authors might have been misled by the fact that their long-slit spectrum was positioned close to kinematic minor axis, where rotation is generally not expected, and covered partly the north-west and south-east region of high-velocity gas visible in the velocity field. This could be the reason for the shape of the velocity curve obtained by MacKenty et al. (1994).

7.4 Knot

A knot located close to the nucleus has been identified on the broad-band images, and named K throughout the paper. It corresponds to the secondary nucleus of the merger hypothesis claimed by MacKenty, who showed its stellar nature by means of an *I*-band *HST* image. The kinematical analysis of our integral-field data confirmed the merger hypothesis: the knot K is a real secondary nucleus, the remnant of a dwarf galaxy which sank into the main disc of the galaxy. In fact, a stellar component kinematically independent from the main galaxy was discovered and its velocity field reconstructed by means of high-resolution integral-field spectra obtained with MPFS. The velocity field clearly shows a rotation pattern lying over the knot K, which has $\Delta V \sim +600\ km\ s^{-1}$ with respect to the systemic velocity of the galaxy.

The high velocity of the impact is expected to produce gas compression. Indeed, this secondary nucleus is embedded in the Hα emission of the galaxy, and it also shows a faint [O III] emission, but is strongly emphasized in the integral-field maps of [O III] λ4363, [O I] λ6300 and [S II] λ6724 emission lines. All these features are a probe that the gaseous component at the location of K is mainly ionized by shocks. In particular, the auroral line [O III] λ4363 ($^1S_0 - {}^1D_2$) can have two main origins. The collisionally populated level $^1S_0$ can be excited by both high electron density or high gas temperature. As the critical density of this transition is around 10^8–$10^9\ cm^{-3}$, in the case of lower density gas, as happens in NLR or generally in H II regions, this line is a function of the temperature. In fact the [O III] 4959+5007/4363 ratio is used as a direct measure of the gas temperature, provided that the electron density $n_e < 10^6\ cm^{-3}$. Therefore [O III] λ4363 is so weak in classical H II regions, with temperatures ranging around 5000–10 000 K, that is generally not observed, while it is visible when $T \sim 10^5$–10^6 K. These are the conditions of SNRs or in general of shock-excited gas.

We stress that the knot K and its surroundings are characterized by higher electron density and internal extinction than the other regions except the nucleus. Moreover, the diagnostic line ratios indicate that this secondary nucleus shares the same properties observed in LINER galaxies. In particular, it satisfies the [O II] λ3727/[O III] λ 5007 $\geqslant$ 1, and [O I] λ6300/[O III] λ 5007 $\geqslant$ 1/3, emission-line ratios criteria proposed by Heckman (1980) and extensively discussed by Ho (2004) to define a LINER. Therefore, we cannot exclude that this knot could be a low-luminosity active nucleus, and if this is the case, Mrk 315 can be numbered as a new case of two active nuclei in merging. Analogous results were obtained by Rifatto et al. (2001) for ESO 202-G 23, and by Komossa et al. (2003) for NGC 6240.

7.5 Filaments

The nature of the filaments mentioned in Section 3 is controversial. F1 and part of F2 were already found and discussed by MacKenty (1986) and MacKenty et al. (1994), who considered them as a single filament with a 'hook' shape. Moreover, MacKenty (1986) could see F1 only in narrow-band filters, and not in continuum light. At the beginning we also obtained a similar result, but later, thanks to

deeper images, we could observe that the situation is completely different: there exist two independent filaments likely crossing in projection, and they are both visible in continuum light.

The shape of F1 could indicate that it is a tidal tail, but there is evidence against this hypothesis. First of all, the gas velocity is much higher than what is expected in the case of a kinematical connection to the main body of the galaxy, as it usually happens with the classical tidal tails (see e.g. Hibbard & van Gorkom 1996, and references therein). Second, radio observations did not find any trace of H I emission in correspondence to the filament. On the other hand, the jet hypothesis was already discussed and discarded by MacKenty (1986). Essentially, the lack of radio emission beyond the boundaries of the galaxy excludes the fact that the filament could be a jet. Indeed, the 6- and 20-cm observations by Nonino et al. (1998) showed only a diffuse emission coincident with the extended regions of star formation found in the quasi-ring, and two bright knots corresponding to the active nucleus N and the secondary nucleus K. Similar narrow and long structures may occur in the case of relativistic jets from active nuclei. The strong magnetic field causes a collimated radio emission with non-thermal spectrum, which should be aligned with its optical counterpart, as is observed in radiogalaxies. Even if the relativistic jet were oriented directly toward us, so we could not observe synchrotron emission, it should become broader at the end owing to the bow shock. This is not the case for F1.

We propose the following possible interpretation for both F1 and F2: they are likely the debris of the interaction between Mrk 315 and two dwarf companions. In particular, one sank into the main galaxy and gave rise to a minor merger event (knot K), while the other passed closed to Mrk 315 in a sort of fly-by (south-east dwarf). It has been demonstrated by simulations and observations, that a satellite companion crossing through the halo of the main galaxy undergoes a tidal interaction, which strips away its outer stars, and forms extended tails with low surface brightness which are usually difficult to detect (Forbes et al. 2003). This idea is close to the hypothesis proposed by MacKenty et al. (1994) and Simkin & MacKenty (2001), that the filament F1 could be '. . .a short-lived wake left behind a bow-shock formed by the passage of the galaxy's nucleus through the neutral gas'.

In F1 the gas trails along the trajectory followed by the dwarf galaxy, and its velocity increases along the filament, in agreement with the long-slit observations by MacKenty et al. (1994). Moreover, its distribution should be curved near the massive core, as we see in the middle-band [O III] images. MacKenty (1986) already observed that extrapolating the filament into the galaxy failed to intersect the nucleus by $\sim$1 arcsec. If we take in account the length of the right side of the filament ($\sim$70 kpc in the projected distance), the falling time is about 1.2×10^8 yr. As this value is three to five times shorter than the period of rotation of Mrk 315, we expect that the filament is not strongly disturbed by differential rotation.

The emission-line ratios available for the part of the filament within the disc of the galaxy (region J1) show an high-ionization degree, probed by the [O III]/Hβ and [O II]/[O III] values, which is similar to those observed in the active nucleus. It is straightforward to claim that nuclear radiation is ionizing the gas along the filament. This was also suggested by Wilson (1988), who measured [O III]/Hβ ratios larger than 3 (and up to 17) in the north-west region of the galaxy.

But energy budget calculations provide a flux of nuclear ionizing photons lower than that requested to sustain such a high-ionization level at large distances from the central engine. Therefore, another additional source must be invoked. As the gas is moving at high velocity along J1, we should reasonably expect that strong shock excitation occurs (Mach number >10), and owing to the low density of the gas, the collisions should cause strong [O III] emission (in analogy with [O III] structures observed in radio galaxies).

8 SUMMARY

In this paper we have presented, analysed and discussed new data about the Seyfert 1.5 galaxy Mrk 315, which allowed us to improve the overall knowledge of this peculiar object. Apparently isolated and undisturbed, Mrk 315 is known to hide interesting features, and this induced previous authors to classify it as a current merger. The analysis of the light distribution in different wavelength ranges of the optical domain, combined with the integral-field spectroscopic information, showed that the galaxy has an early-type spiral morphology, with an inner and an outer disc. The inner disc shows bright star-forming regions arranged in a quasi-ring around the nucleus, and it hosts a secondary nucleus close to the AGN, centre of mass of a dwarf galaxy remnant, which sank into the main body of the galaxy, producing clear effects of gas compression and shock ionization. Highly ionized and collimated gas is observed to move radially at high velocity with respect to the rotation of the galaxy, and in agreement with the velocity of the secondary nucleus. This gas is connected to a giant filament. We have discussed the nature of this filament, excluding the tidal tail and/or jet hypotheses, and propose the idea of debris of the dwarf galaxy, which passed through the halo of the main galaxy loosing stars and gas. We also identified a second and more extended filament, to which we ascribed a similar origin. This filament is clearly connected to an emission-line dwarf galaxy, which has a redshift in agreement with that of Mrk 315, and is associated with a bright H I cloud.

ACKNOWLEDGMENTS

We are grateful to the anonymous referee for precious comments and suggestions which improved the quality of the paper. We are also grateful to Professor S. Simkin and Professor V. Reshetnikov for useful discussions. A. Moiseev thanks the Russian Science Support Foundation.

This work was based on observations carried out at the 6-m telescope of the Special Astrophysical Observatory of the Russian Academy of Sciences, operated under the financial support of the Science Department of Russia (registration number 01–43).

This research has made use of the NED which is operated by the Jet Propulsion Laboratory, California Institute of Technology, under contract with the National Aeronautics and Space Administration.

This research was partly based on data from the ING Archive.

REFERENCES

Afanasiev V. L., Moiseev A. V., 2005, Astron. Lett., 31, 193
Afanasiev V. L., Dodonov S. N., Moiseev A. V., 2001, in Ossipkov L. L., Nikiforov I. I., eds, Proc. Int. Conf. Stellar Dynamics: from Classic to Modern. Sobolev Astron. Inst. St Petersburg, p. 103
Athanassoula E., Puerari I., Bosma A., 1997, MNRAS, 286, 284
Bachev R., Strigachev A., Dimitrov V., 2000, A&AS, 147, 175
Begeman K. G., 1989, A&A, 223, 47
Bell E. F., 2003, ApJ, 586, 794
Bushouse H. A., 1986, AJ, 91, 255
Cardelli J. A., Clayton G. C., Mathis J. S., 1989, ApJ, 345, 245
Carollo C. M., Stiavelli M., Mack J., 1998, AJ, 116, 68
Chapman S. C. et al., 2000, MNRAS, 319, 318
Chatzichristou E. T., 2000, ApJS, 131, 71
Chatzichristou E. T., 2001, ApJ, 556, 653

Ciroi S., Contini M., Rafanelli P., Richter G. M., 2003, A&A, 400, 859
Condon J. J., Yin Q. F., 1990, ApJ, 357, 97
Dahari O., 1984, AJ, 89, 966
De Robertis, Yee H. K. C., Hayhoe K., 1998, ApJ, 496, 93
Erwin P., Beltrán J. C. V., Graham A. W., Beckman J. E., 2003, ApJ, 597, 929
Forbes D. A., Beasley M. A., Bekki K., Brodie J. P., Strader J., 2003, Sci, 301, 1217
Fuentes-Williams T., Stocke J. T., 1988, AJ, 96, 1235
Fukugita M., Ichikawa T., Gunn J. E., Doi M., Shimasaku K., Schneider D. P., 1996, AJ, 111, 1748
Heckman T. M., 1980, A&A, 87, 152
Heckman T. M. et al., 2005, ApJ, 619, L35
Hernquist L., Mihos J. C., 1995, ApJ, 448, 41
Hibbard J. E., van Gorkom J. H., 1996, AJ, 111, 655
Ho L. C., Shields J. C., Filippenko A. V., 1993a, ApJ, 410, 567
Ho L. C., Filippenko A. V., Sargent W. L. W., 1993b, ApJ, 417, 63
Ho L. C. W., 2004, ed., Carnegie Observatories Astrophysics Series, Vol. 1, Coevolution of Black Holes and Galaxies. Cambridge Univ. Press, Cambridge, p. 293
Huchra J., Sargent W. L. W., 1973, ApJ, 186, 433
Kennicutt R. C., 1998, ARA&A, 36, 189
Komossa S., Schulz H., 1997, A&A, 323, 31
Komossa S., Burwitz V., Hasinger G., Predehl P., Kaastra J. S., Ikebe Y., 2003, ApJ, 582, L15
Kormendy J., 1982, ApJ, 257, 75
Koski A. T., 1978, ApJ, 223, 56
Laurikainen E., Salo H., Teerikorpi P., Petrov G., 1994, A&AS, 108, 491
MacKenty J. W., 1986, ApJ, 308, 571
MacKenty J. W., 1989, ApJ, 343, 125
MacKenty J. W., Simkin S. M., Griffiths R. E., Ulvestad J. S., Wilson A. S., 1994, ApJ, 435, 71
Mannucci F. et al., 2003, A&A, 401, 519
Martini P., Regan M. W., Mulchaey J. S., Pogge R. W., 2003, ApJ, 589, 774
Mazzarella J. M., Bothun G. D., Boroson T. A., 1991, AJ, 101, 2034
Mihos J. C., Hernquist L., 1994, ApJ, 425, L13
Mihos J. C., Hernquist L., 1996, ApJ, 464, 641
Miller C. J., Nichol R. C., Gómez P. L., Hopkins A. M., Bernardi M., 2003, ApJ, 597, 142
Mirabel I. F., Wilson A. S., 1984, ApJ, 277, 92
Moiseev A. V., 2002, Bull. Special Astrophys. Obs., 54, 74
Moiseev A. V., Valdés J. R., Chavushyan V. H., 2004, A&A, 421, 433
Moriondo G., Giovanardi C., Hunt L. K., 1998, A&AS, 130, 81
Neff S. G., Ulvestad J. S., Teng S. H., 2004, ApJ, 611, 186
Nonino M., Henry J. P., Fanti C., Fanti R., Davies J., 1998, MNRAS, 299, 332
Osterbrock D. E., 1989, Astrophysics of Gaseous Nebulae and Active Galactic Nuclei. University Science Books, Mill Valley CA
Penston M. V. et al., 1990, A&A, 236, 53
Pizzella A., Corsini E. M., Morelli L., Sarzi M., Scarlata C., Stiavelli M., Bertola F., 2002, ApJ, 573, 131
Pogge R. W., Martini P., 2002, ApJ, 569, 624
Radovich M., Hasinger G., Rafanelli P., 1998, AN, 319, 325
Radovich M., Ciroi S., Contini M., Rafanelli P., Afanasiev V. L., Dodonov S. N., 2005, A&A, 431, 813
Rafanelli P., Violato M., Baruffolo A., 1995, AJ, 109, 1546
Reshetnikov V., Combes F., 1999, A&AS, 138, 101
Rifatto A., Rafanelli P., Ciroi S., Radovich M., Vennik J., Richter G., Birkle K., 2001, AJ, 122, 2301
Rowan-Robinson M. et al., 1997, MNRAS, 289, 490
Sargent W. L. W., 1970, ApJ, 160, 405
Schmitt H., 2001, AJ, 122, 2243
Sérsic J. L., 1968, Atlas de Galaxies Australes
Sil'chenko O. K., Afanasiev V. L., 2000, A&A, 364, 479
Sil'chenko O. K., Vlasyuk V. V., Alvarado F., 2001, AJ, 121, 2499
Simien F., de Vaucouleurs G., 1986, ApJ, 302, 564
Simkin S. M., MacKenty J. W., 2001, in Hibbard J. E., Rupen M. P., van Gorkom J. H., eds, Proc. ASP Conf. Vol. 240, Gas and Galaxy Evolution, A Conference in Honor of the 20th Anniversary of the VLA. Astron. Soc. Pac., San Francisco, p. 408
Smith H. E., Lonsdale C. J., Lonsdale C. J., 1998, ApJ, 492, 137
Taniguchi Y., 1999, ApJ, 524, 65
van den Bergh S., Tammann G. A., 1991, ARA&A, 29, 363
Veilleux S., Osterbrock D. M., 1987, ApJS, 63, 295 (VO)
Wilson A. S., 1988, Adv. Space Res., 8, 27
Wozniak H., Combes F., Emsellem E., Friedli D., 2003, A&A, 409, 469
Zaritsky D., Smith R., Frenk C., White S. D. M., 1997, ApJ, 478, 39

This paper has been typeset from a TEX/LATEX file prepared by the author.